BIOMEDICAL ENGINEERING MSc PROGRAM
UNIVERSITY OF CRETE
TECHNICAL UNIVERSITY OF CRETE
FOUNDATION FOR RESEARCH AND TECHNOLOGY-HELLAS

University of Crete

Medical School

Biomedical Engineering MSc Program

"Visible Light Photopolymerizable Hydrogels: Synthesis, Characterization and *In Vitro* Evaluation"

Anna Papaioannou

Supervising Professors: Maria Vamvakaki, Maria Chatzinikolaidou

Evaluation Committee: Maria Vamvakaki, Maria Chatzinikolaidou, Anna Mitraki

Heraklion 2023

Πανεπιστήμιο Κρήτης

Ιατρική Σχολή

ΔΠΜΣ στη Βιοϊατρική Μηχανική

“Πολυμερισμός Υδρογελών με Ορατό Φως: Σύνθεση, Χαρακτηρισμός and *In Vitro* Αξιολόγηση”

Άννα Παπαϊωάννου

Επιβλέπουσες Καθηγήτριες: Μαρία Βαμβακάκη, Μαρία Χατζηνικολαΐδου

Τριμελής Επιτροπή: Μαρία Βαμβακάκη, Μαρία Χατζηνικολαΐδου, Άννα Μητράκη

Ηράκλειο 2023

Acknowledgements

I would like to thank everyone that supported me throughout the completion of my master's thesis.

First of all, I would like to express my deep appreciation and gratitude to Prof. Maria Vamvakaki as my supervisor, for her guidance, support and patience during my first steps in this new and exciting field of polymer chemistry. I would also like to thank Prof. Maria Chatzinikolaidou, for supervising the *in-vitro* experiments, for her valuable advice and excellent collaboration in an integral part of my thesis, and also Prof. Anna Mitraki for honoring me with her participation in the evaluation committee.

I am also very thankful to Dr. Eva Vasilaki for her patience, for all the things that I learned working by her side but most of all for her understanding. I would also like to thank Mrs. Danai Papadogianni and PhD Candidate Konstantinos Loukelis, for their collaboration and for conducting the biological evaluation experiments.

I want to thank Dr. Maria Kalyva, Dr. Theodoros Manouras, and PhD Candidate Maria Psarrou for their support. I am very grateful for the family we built with the rest of the lab members Dimitris, George K., Rania, Dimitra, Myrto, Marianna, Vassilis, Sofia and George P., supporting each other throughout this past year and a half.

I could not possibly forget to thank my friends and my family for their love and their encouragement. And the biggest thank you goes to Vassilis T. for always being there ,and for believing in me in every step of the way.

Thank you all!

Table of Contents

Abstract

Hydrogels have been widely used in biomedical applications, such as drug delivery and tissue engineering. Their unique properties, providing a large network of pores for cell encapsulation and the permeation of nutrients, their high degrees of swelling and water absorption and the tunability of their mechanical properties, have established them as excellent candidates for use as tissue engineering scaffolds. Hydrogel synthesis via photo-polymerization/photo-cross-linking is an advantageous method enabling fast reaction rates, in-situ gel formation at physiological temperatures and a spatiotemporal control of the hydrogel formation process. The main disadvantage of the photo-polymerization/photo-cross-linking process lies in the use of UV light for photo-initiation/ photo-cross-linking, which can be toxic for the cells and have adverse effects to the cell's metabolic activity, thus preventing its use in photo-polymerizable bioinks. To address this problem, the development of systems that can undergo photo-polymerization/photo-cross-linking under visible light is highly desired.

In this thesis, we explore the synthesis of polymer hydrogels for use as tissue engineering scaffolds, using g-C_3N_4 as a novel visible light photo-initiator. Biodegradable hydrogels presenting a favorable environment for cell attachment and proliferation, were synthesized using gelatin methacrylamide (GelMA) and dopamine methacrylamide (DMA) as the comonomers. The GelMA-*co*-DMA hydrogels were prepared by photo-initiated polymerization/photo-cross-linking, using g-C_3N_4, in the absence of an additional cross-linker. The as-synthesized hydrogels exhibited swelling and degradation profiles which were dependent on their GelMA and DMA composition. Finally, composite hydrogels incorporating nanohydroxyapatite were synthesized and investigated as biodegradable 3D scaffolds for bone tissue engineering applications.

Περίληψη

Οι υδρογέλες (hydrogels) έχουν χρησιμοποιηθεί ευρέως σε βιοϊατρικές εφαρμογές, όπως η μεταφορά φαρμάκων και η μηχανική ιστών. Οι μοναδικές ιδιότητές τους, όπως η πορώδης μορφολογία τους με μεγάλο για την ενθυλάκωση κυττάρων και τη διαπερατότητα θρεπτικών ουσιών, οι υψηλοί βαθμοί διόγκωσης (swelling) και προσρόφησης νερού και η δυνατότητα ρύθμισης των μηχανικών τους ιδιοτήτων κατά τη σύνθεσή τους, τα έχουν καθιερώσει ως εξαιρετικά υλικά για τη χρήση τους ως ικριώματα μηχανικής ιστών. Η σύνθεση υδρογελών μέσω φώτο-πολυμερισμού (photo-polymerization) είναι μία πλεονεκτική μέθοδος που επιτρέπει γρήγορους ρυθμούς αντίδρασης, το σχηματισμό in situ σε φυσιολογικές θερμοκρασίες και το χώρο-χρονικό έλεγχο της διαδικασίας σχηματισμού της υδρογέλης. Το κύριο μειονέκτημα της διαδικασίας φώτο-πολυμερισμού έγκειται στη χρήση υπεριώδους (UV) ακτινοβολίας για τη φώτο-εκκίνηση (photo-initiation), η οποία μπορεί να είναι τοξική για τα κύτταρα και να έχει δυσμενείς επιδράσεις στη μεταβολική δραστηριότητα των κυττάρων, εμποδίζοντας έτσι τη χρήση τους ως φώτο-πολυμεριζόμενα μελάνια (photopolymerizable bioinks) για τη δημιουργία ικριωμάτων. Για την αντιμετώπιση αυτού του προβλήματος, είναι ιδιαίτερα επιθυμητή η ανάπτυξη συστημάτων φώτο-πολυμερισμού υπό ορατό φως.

Στην παρούσα εργασία, διερευνούμε τη σύνθεση πολυμερικών υδρογελών για χρήση ως ικριώματα μηχανικής ιστών, χρησιμοποιώντας το g-C_3N_4 ως νέο φώτο-εκκινητή υπό ορατό φως. Βιοδιασπώμενες υδρογέλες που παρουσιάζουν ένα ευνοϊκό περιβάλλον για την προσκόλληση και τον πολλαπλασιασμό των κυττάρων, συντέθηκαν χρησιμοποιώντας ζελατίνη (GelMA) και ντοπαμίνη (DMA) ως συνθετικά. Οι συμπολυμερικές υδρογέλες GelMA-*co*-DMA παρασκευάστηκαν με φώτο-πολυμερισμό, χρησιμοποιώντας το g-C_3N_4 ως εκκινητή, απουσία πρόσθετου διασταυρωτή και οι ιδιότητες διόγκωσης (swelling) και αποικοδόμησης (degradation) των υδρογελών εξαρτώνται από τη σύσταση τους, τόσο από τις συγκεντρώσεις των GelMA και DMA, όσο και από το βαθμό τροποποίησης της ζελατίνης και το χρόνο έκθεσης. Τέλος, συντέθηκαν νάνο-σύνθετες πολυμερικές υδρογέλες με νάνο-υδρόξυ-απατίτη ως βιοαποικοδομήσιμα τρισδιάστατα ικριώματα και διερευνήθηκαν για την εφαρμογή τους για τη μηχανική οστίτη ιστού.

Chapter 1: Introduction

1.1 Hydrogels

Hydrogels is a class of cross-linked polymers that form three dimensional networks and can absorb large amounts of water without dissolution. Due to their excellent properties, including the permeation of oxygen, nutrients and metabolites, as well as the tunability of their mechanical strength and degradation, hydrogels have been established as excellent materials for use in various fields, such as in biomedical applications[1,2] as contact lenses[3], biosensors[4], drug carriers[5] and tissue engineering scaffolds[6,7].

1.1.1 Hydrogel classification based on the polymer origin

Hydrogels can be classified as either natural or synthetic, as depicted in Figure 1.1, depending on the nature of the monomers or polymers used for their synthesis. Natural hydrogels are synthesized using natural polymers such as nucleic acids, polysaccharides, proteins, etc. Collagen[8,9], gelatin[10,11], chitosan[12,13], hyaluronic acid[14,15], alginate[16,17], and heparin[18,19] are some of the most commonly employed natural polymers in hydrogel synthesis. Due to their inherent biodegradability and biocompatibility, natural polymers are very promising candidates for bio-related applications, such as tissue engineering and drug delivery.[6,20] Accordingly, synthetic hydrogels are prepared using synthetic polymers. The properties of a synthetic hydrogel can be tuned during polymer synthesis, as the polymer can be synthesized and functionalized to fit the prerequisites of the application.[21] The most common examples of synthetic polymers used in hydrogel synthesis are poly(ethylene glycol) (PEG)[22,23], polyacrylamides[24,25], poly(lactic acid) (PLA)[26,27] and poly(glycolic acid)[28,29], poly(lactic-co-glycolic acid) (PLGA)[27,30], poly(vinyl alcohol)[13,31] and other biodegradable polyesters[21]. Hybrid hydrogels can be also synthesized, by combining both natural and synthetic polymers to obtain materials with beneficial properties for the intended applications.[21,32,33]

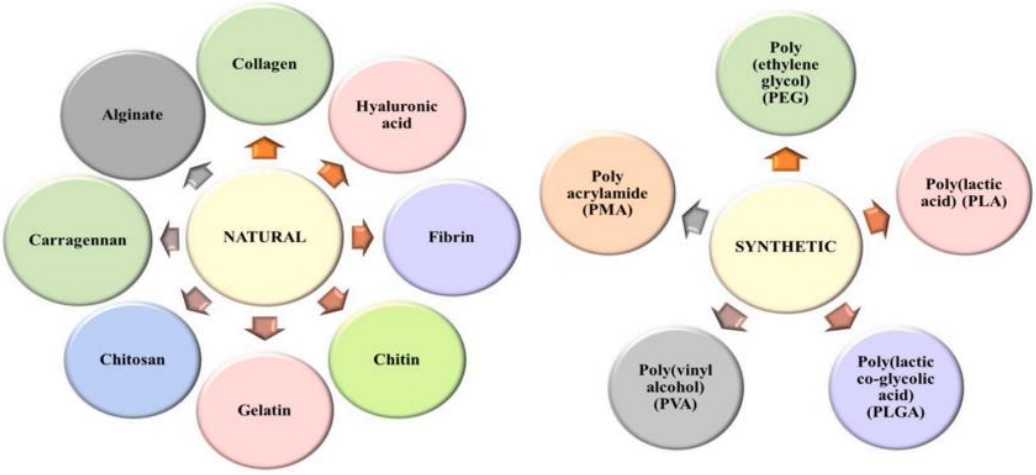

Figure 1.1 – Classification of hydrogels based on the polymer origin.[32]

1.1.2 Hydrogel classification based on other parameters

Hydrogels can be further classified according to the nature of the cross-links forming the hydrogel network, as either chemical or physical. Chemical hydrogels, formed via covalent bonds between the polymer chains, are irreversible, while physical hydrogels formed by hydrogen bonding, hydrophobic interactions, coordination bonding, etc., among the polymer chains, can be reversible when the gel is exposed to different environmental conditions (e.g., temperature, salt concentration, pH, irradiation). Hydrogels that respond to external stimuli, also known as responsive hydrogels, can be further classified based on the environmental cues that trigger their response. These cues can be either chemical, such as the pH or the presence of oxidants, physical, like temperature or light irradiation, or biochemical, such as the presence of an enzyme or an antigen.[34]

Hydrogels can also be categorized according to their preparation conditions as homopolymer, when only one type of monomer is used, or copolymer, if two types of monomers are used, and finally, as interpenetrating when two networks of different polymers are formed in the hydrogel structure, resulting in enhanced mechanical properties among other. In addition, depending on the ionic charge of the monomer(s)/polymer(s) used in hydrogel synthesis, the latter can be cationic, anionic, or non-ionic.[34]

Over the years, hydrogel synthesis has evolved from employing simple synthetic procedures to cross-link hydrophilic polymers, towards the introduction of multiple functionalities. Thus, hydrogels can nowadays be classified as either conventional or "smart", depending on the functionalities introduced into the system. [35]

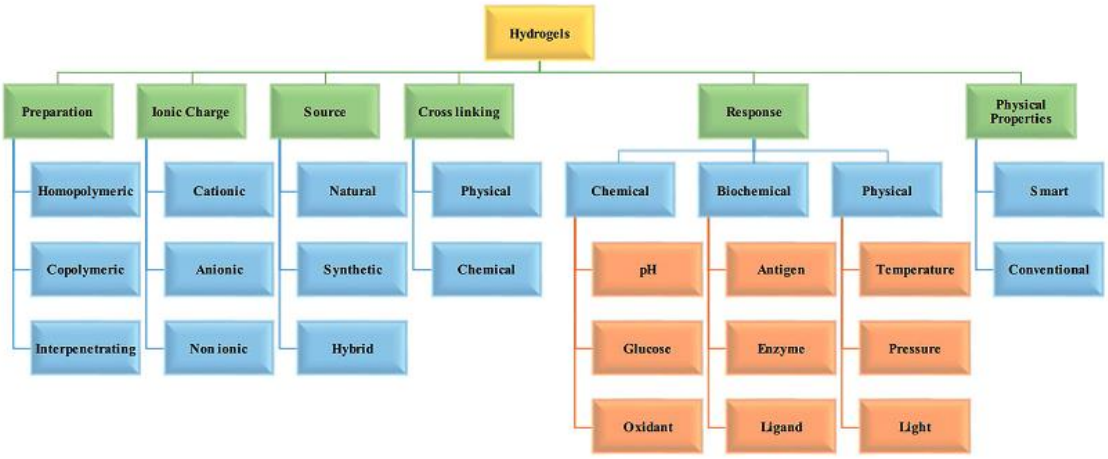

Figure 1.2 – Classification of hydrogels.[34]

1.1.3 Hydrogels in biomedical applications

Materials that are suitable for biomedical applications, also known as biomaterials, must satisfy certain specific requirements. Biocompatibility is the most important property among them. A material is considered biocompatible if it has the "ability to perform with an appropriate host response in a specific situation"[36]. Thus, the material should co-exist with living cells or the surrounding tissue in a mutually acceptable manner, with a minimal to no immune response. Minimum to no toxicity and no tumorigenicity are also prerequisites in biomedical applications.[37] Hydrogels have emerged as great representatives in this field of research.

The use of hydrogels in biomedical applications has sparked the research interest since the 1960s, when Wichterle and Lim first proposed the term "hydrogel", in their paper entitled "*Hydrophilic gels for biological use*", introducing poly(hydroxyethyl methacrylate) (pHEMA) hydrogels with the potential to be applied as soft contact lenses.[38] Due to their inherent properties such as extreme hydrophilicity, water swelling and retention, metabolite permeation and soft rubbery consistency, hydrogels represent

a class of materials closely resembling living tissues. These merits have established them as excellent candidates in various biomedical fields, and especially in drug delivery and tissue engineering.

1.1.3.1 Hydrogels as tissue engineering scaffolds

Tissue Engineering (TE) emerged in the late 1980s as an interdisciplinary field with the aim to create novel therapies addressing the treatment of diseased or damaged tissue. By definition, TE refers to "the application of the principles and methods of engineering and life sciences toward the fundamental understanding of structure-function relationships in normal and pathological mammalian tissue and the development of biological substitutes to restore, maintain, or improve tissue function".[39] In order for the aforementioned targets to be achieved, the combination of multiple research and engineering fields is required. The three essential elements that have helped to advance this field are cells, signals and scaffolds, also known as the "tissue engineering triad".[40]

Scaffolds play the important role of a temporary "home" for the cells, and as such there are specific traits that are considered as prerequisites for such materials. Among the different materials used and engineered to serve as scaffolds for TE (metals, alloys, ceramics, and polymers)[41], hydrogels possess some inherent properties that render them superior to the other candidates. Their high and tissue-like water content and their porous structure can facilitate nutrient and oxygen permeation and metabolite excretion, while their 3-dimensional structure that effectively simulates the 3D-environment of the extracellular matrix, can promote cell attachment and proliferation.[42] Moreover, the hydrogels' mechanical and other properties can be tuned during synthesis, to provide mechanical and other stimuli that promote differentiation, while simultaneously, chemical signals can be facilitated by the incorporation of growth factors that can be released from the hydrogel. [42]

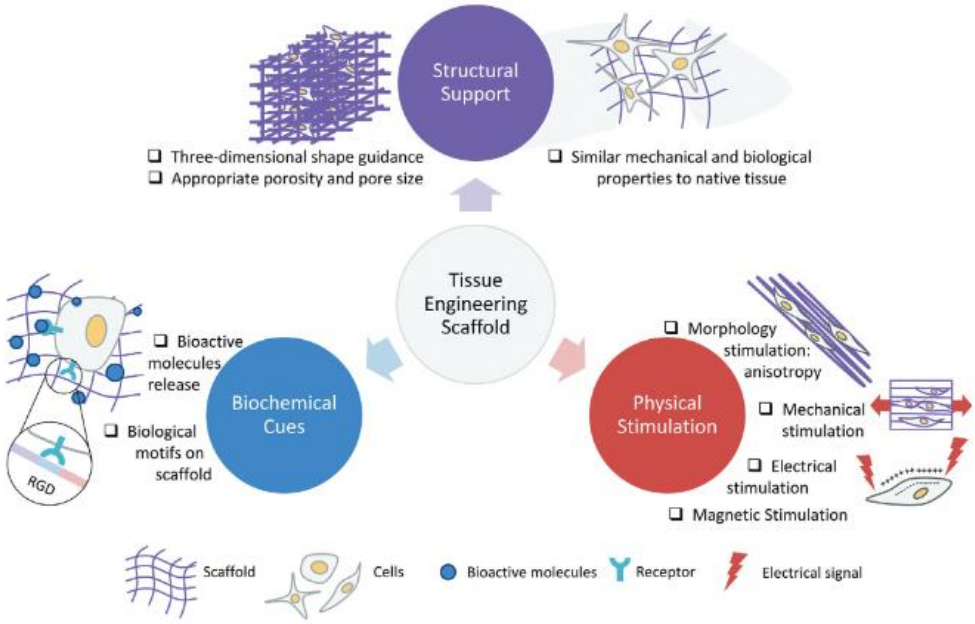

Figure 1.3 – Design Parameters for Tissue Engineering Scaffolds.[21]

TE approaches using hydrogels involve, either the formation of the hydrogel followed by cell seeding *in vitro* prior to *in vivo* implantation, or the direct injection of the hydrogel-cell suspension as a liquid and the in-situ gelation inside the targeted tissue.[43] In either case, the material that enters the body should be, as already mentioned, biocompatible, as well as biodegradable.[39] Biodegradability can be ensured during synthesis, by employing natural polymers that are inherently biodegradable, or by systematically designing synthetic polymers that bear biodegradable bonds, such as polyesters or polyamides.[21] During biodegradation the scaffold loses its structural integrity, and its mechanical strength is compromised, thus the degradation rate has to be tuned to match the rate of tissue formation.[39] The rate of degradation can be controlled by the polymer molecular weight and the cross-link density of the synthesized hydrogel.[42]

1.1.3.2 Collagen and gelatin hydrogels for TE

Collagen is one of the most abundant protein materials in the human body being one of the main typical components of the extracellular matrix. Due to its protein sequence,

Gly-X-Y, it forms a left handed α-triple helix, which contributes to its final fibrous morphology.[44] Cellular adhesion and proliferation are promoted in constructs containing collagen, since the RGD peptide sequence that is present in its primary amino acid chain acts as a binding site for cells.[45] Although it is an excellent biomaterial, collagen lacks in mechanical properties and is readily degraded by enzymes, as is the case for most natural polymers.[21] Nevertheless, scientists have proposed several combinations of collagen with other materials that can be beneficial to the integrity and the mechanical properties of collagen derived hydrogels, as for example the incorporation of synthetic polymers[8,46,47] or even nanomaterials[9,48]. Ji et al. proposed the combination of collagen with poly(ethylene glycol fumarate) (PEGF), a functionalized derivative of PEG, with alternating fumaric acid and PEG units, in interpenetrating hydrogel networks as a scaffold for soft tissue engineering with enhanced mechanical and degradation properties.[8] The presence of collagen in the constructs improved the *in vitro* response of NIH-3T3 fibroblasts to scaffold extracts, while increasing concentrations of PEGF improved the stability of the hydrogels against collagenase solution. Increasing concentrations of PEGF also awarded the synthesized hybrid hydrogels with improved mechanical properties, leading to a two-fold increase of the compressive modulus for hybrid hydrogels containing 2% collagen-16% PEGF compared to the modulus exhibited by natural 2% collagen hydrogels. Sun et al. demonstrated the enhanced mechanical and electrical properties of collagen hydrogels incorporating carbon nanotubes (CNTs) for cardiac tissue engineering.[9] Increasing filler concentrations lead to mechanical reinforcement of the nanocomposite hydrogels, yielding a 30 kPa compressive modulus for 2 wt% concentration of CNTs in the hydrogels, significantly higher to that of the bare collagen hydrogel, approximately equal to 15 kPa. Incorporation of CNTs was also evidenced to promote cell adhesion and alignment in confocal images of neonatal rat ventricular myocytes (NRVMs) and was also proven to be beneficial and enhance the cardiac construct functionality with improved and increased beating frequency of constructs based on the nanocomposite hydrogels. Tatiana et al. proposed the synthesis of hybrid collagen/pNIPAM nanocomposite hydrogels incorporating hydroxyapatite for bone tissue engineering with improved resistance to enzymatic degradation and enhanced thermal stability.[47]

Gelatin, as the hydrolyzed form of collagen, has a similar primary structure and thus bears all the favorable properties of its precursor, such as excellent biocompatibility and biodegradability.[49] Due to the hydrolysis though, the helical secondary structure of collagen is not retained, rendering gelatin inferior to collagen in terms of mechanical properties and solubility.[50] Gelatin also exhibits thermo-reversible gelation at 37 ^{o}C[51] and poor degradation properties at physiological temperatures[52], and thus its stability and enhanced performance can only be ensured by cross-linking its polymer chains. To that end, gelatin can be very easily functionalized[53,54] and the degree of functionalization of the polymer can be tuned to obtain hydrogels with fast gelling properties, enhanced stability and improved mechanical integrity.[10,55] Other advantages of gelatin over collagen also include its relatively low cost and wide availability.[50]

1.1.3.2 Catechol-functionalized hydrogels for TE

Hydrogel scaffold adhesion in high water-content tissues is hindered by several factors, such as the formation of hydration layers between the biomaterial-tissue interface, preventing the contact between adhesive moieties on the scaffolds and biological surfaces, the damage to non-covalent interactions by water molecules and finally swelling and deswelling of the hydrogels.[56] Conventional approaches to secure the position of scaffolds onto the diseased site, such as sutures, tissue sealants and bio glues, have faced several limitations, such as toxicity of commercial glues, secondary damages cause by sutures, interference with scaffold degradation and inability of most tissue adhesives to support crucial cellular activities related to tissue regeneration.[57] Inspired by the mussel adhesive proteins (maps), and the predominant role of catechols in the underwater adhesion of mussels[58], catechol-functionalized hydrogels and their special adhesive properties have raised scientific interest in the field of self-adhesive hydrogel scaffolds for tissue engineering[26,30,59–63].

Han et al. proposed a mussel inspired polydopamine (PDA) - chondroitin sulfate (CS) – polyacrylamide (PAM) hydrogel as a tissue adhesive growth-factor-free scaffold for cartilage regeneration.[64] The incorporation of polydopamine in the hydrogel network, equipped the scaffolds with exceptional tissue adhesive properties and promoted cell attachment and spreading. Tissue adhesiveness was demonstrated by tensile-adhesion

testing on porcine skin and an exceptional adhesion strength in the range of 25 -30 kPa was achieved for PDA-containing scaffolds, far greater than that of non-PDA-containing hydrogels and that of commercially available glue (15kPa). Immediate and effective binding of the PDA-CS-PAM hydrogel to the surrounding tissue was also observed in the *in vivo* defect repair experiments performed on Japanese white rabbits, ensuring great tissue integration. Zhao et al. also developed a mussel mimetic dual-cross-linked hydrogel containing a dynamically cross-linked system based on pre-assembled boronate ester bonds between nitro-dopamine methacrylamide (nDMA) and 3-acrylamido phenyl boronic acid (AAPBA) to address the poor mechanical properties of mussel inspired tissue adhesive hydrogels.[63] The reversible cross-links present in the hydrogel network served, not only as an efficient energy dissipation mechanism, but also enhanced hydrogel toughness awarding the nDMA/AAPBA hydrogels with an impressive ultimate stress of 0.96 MPa at 90% strain and a compressive modulus of 45 kPa, three times higher than that of the plain nDMA hydrogels. At the same time, adhesion energy to biological tissues, was determined by a 180° peeling test and was estimated to exceed 400 J m^{-2} for nDMA/AAPBA, achieving a two-fold higher adhesion energy compared to the commercially available cyanoacrylate super glue (20-200 J m^{-2}) establishing the superior adhesive properties of catechol-containing hydrogels.

Tissue adhesive properties of hydrogel scaffolds are not only essential to the secure positioning and successful tissue integration of the scaffold, but are also crucial for the regulation of cell function, such as migration, proliferation and differentiation.[65,66] Chakka et al. modified the surface of 3D-printed PLA scaffolds with PDA and determined the osteogenic differentiation ability of dental pulp stem cells (DPSCs) on the fabricated scaffolds.[26] PDA surface modification of the scaffolds was achieved by incubation of the PLA scaffolds in dopamine alkaline buffer solution (10 mM Tris, pH~8) for 30 min – 24 h to induce the dopamine self-assembly onto the surface of the scaffolds. The functionalized scaffolds exhibited improved wettability and a gradual decrease in contact angle from 47° to 20° to 6° for incubation times equal to 10 min, 30 min and 2 h, respectively. Prolonged incubation for 24 h led to a subsequent increase of the contact angle to 26°, still significantly lower than the 87° measured for the

untreated PLA scaffold. PLA-PDA scaffolds incubated for 2 h showed enhanced cell proliferation and greater osteogenic differentiation potential of DPSCs compared to the untreated counterparts[26] as improved wettability is associated with enhanced cell attachment and spreading and thus greater proliferation potential.[67] Li et al. employed a similar approach for the incorporation of polydopamine to enhance cell adhesion and proliferation on PLGA scaffolds.[30] PLGA electrospun fibers were surface modified with PDA by immersion in dopamine solution (pH~8.5) under stirring for 6 h. Chitosan (CS) and gelatin (Gel) were incorporated into the scaffolds via immersion of the PLGA/PDA scaffolds in CS or Gel solution and subsequent immersion in liquid nitrogen for 1 h before freeze-drying. Enhanced hydrophilicity was observed in water-contact angle measurements for all PDA-containing scaffolds, as well as improved cell proliferation both for MC3T3-E1 and rat bone marrow-derived stromal cells (rBMSCs). SEM images of cells after 7 days in cell culture revealed a significant increase in cell population and cell spreading areas for both MC3T3-E1 and rBMSCs on the PDA-containing scaffolds. Vinculin staining, used as a focal adhesion marker in confocal immunofluorescence images, exhibited elevated levels of expression on PLGA/PDA scaffolds and was correlated with higher levels of cell adhesion for both cell types, ensuring the positive effect of dopamine on cell adhesion.

Apart from the introduction of bio-functional properties, catechol functionalization has also been employed for the mineralization of scaffolds in bone tissue engineering.[22,59,68] Employing the strong binding affinity of catechols for metal cations, Liu et al. synthesized a dopamine-modified PEG nanocomposite hydrogel.[22] They proposed the incorporation of Laponite ® in the hydrogel network via reversible physical bonds with the dopamine moieties of the PEG chains, providing the hydrogel with additional physical cross-links. Laponite-incorporated hydrogels exhibited an increase in the elastic modulus, elevated fracture strains and improved cellular infiltration levels in the *in vivo* subcutaneous implantation experiments contacted on Sprague-Dawley rats. Another mussel inspired bilayer gelatin hydrogel for osteochondral repair, with PDA induced hydroxyapatite (nHAp) mineralization in the upper layer, was proposed by Gan et al.[59] In situ mineralization of the gelatin hydrogel was achieved by dissolving dopamine and $Ca(NO_3)_2/(NH_4)_2HPO_4$ in the designated ratio of 3:1 in the prepolymer

solution, in the presence of ammonium persulfate and by adjusting the pH at 11. The formation of nHAp was enabled in the presence of PDA by catechol-Ca^{2+} binding and nucleation of nanoparticles by the coprecipitation of Ca^{2+} and PO_4^{3-}. The proliferation and chondrogenic differentiation of bone mesenchymal stem cells was evaluated on the mineralized hydrogels. Increased proliferation was noted from day 1 of cell culture for the PDA-containing hydrogels compared to the non-PDA-containing, suggesting the improved cell adhesion onto the catechol-functionalized scaffolds. The presence of HA in the PDA-mineralized hydrogels induced an overall enhanced osteogenic differentiation response of the cells in all the measured markers, further establishing the catechol anchoring and mineralization properties for bone tissue engineering applications.

1.1.4 Hydrogel preparation and cross-link-ing approaches

Hydrogel formation can be achieved by employing two different strategies, namely the in-situ cross-linking and the post-cross-linking approaches. The in-situ cross-linking can be either chemical or physical and can be achieved by the simultaneous polymerization and cross-linking of multifunctional monomers, or in the case of monofunctional monomers by employing a multifunctional cross-linker. The post cross-linking methods refer to the formation of a hydrogel network by reacting a polymer that was synthesized to bear reactive functional groups with suitable cross-linkers. [35]

Free radical polymerization is the most common strategy for the in-situ hydrogel formation. The free radicals are derived from an initiator via thermal or photochemical homolytic cleavage, or by a redox reaction. These radicals then attack the unsaturated bonds of the monomer, giving primary propagating radicals and propagating further the reaction. Cross-linking usually happens in the propagation step of the polymerization reactions and gelation kinetics may vary depending on the bulkiness and the number of unsaturated bonds of the monomer. Termination occurs in the event of combination or disproportionation of the remaining radicals. [69]

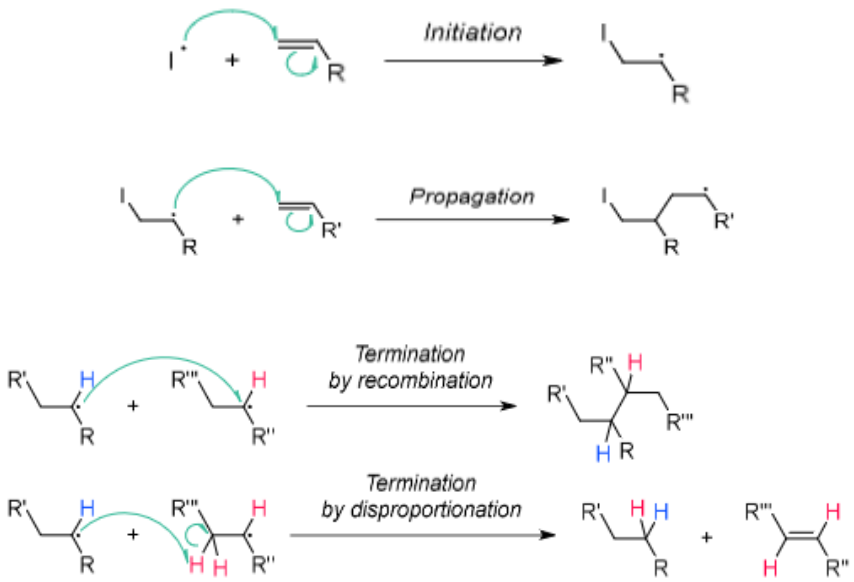

Figure 1.4 – Free Radical Polymerization.[69]

1.2 Photopolymerization

Polymerizations that are initiated using UV or visible light require the presence of an initiator that can produce radicals upon light irradiation of specific wavelength and monomers that bear unsaturated bonds that can be targeted by the initiating radicals. [70]

Photoinitiator molecules have been classified by their mechanism of action as Type I and Type II photoinitiators.[7] Type I photoinitiators consist of molecules that bear bonds that can undergo cleavage when irradiated. This class of materials contains compounds that bear aromatic carbonyl units, such as benzoin or acetophenone derivatives. Upon activation of these groups by light irradiation, homolytic cleavage of the excited α-carbon bond is performed and two radical species are produced as a result [7] (Eq 1.1). Type II photoinitiators are molecules that reach an activated state when irradiated and, in this state, they can produce radicals through the mechanism of hydrogen abstraction, by attracting hydrogen atoms from other donor molecules (co-initiator) (Eq 1.1). Aromatic ketones such as benzophenone and thioxanthone can promote hydrogen abstraction when irradiated with UV light while tertiary amines, alcohols, ethers, and thiols are the most common co-initiators.[7] Apart from photoinitiators, sometimes a

photosensitizer is also used. In specific, photosensitizers are molecules that can be excited by light absorption and act as intermediates to transfer the excitation to the photoinitiator either by energy (Eq 1.2) or electron transfer (Eq 1.3). [71]

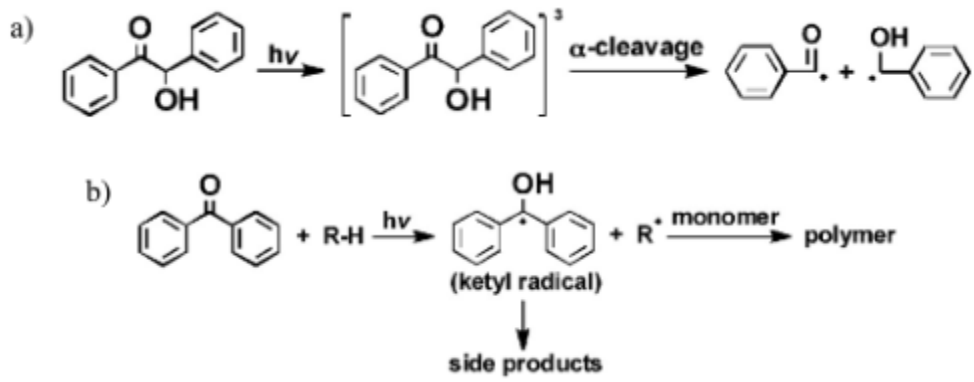

Figure 1.5 –Photoinitiator Type Mechanism (a) photolytic cleavage of benzoin, a type I photoinitiator, and (b) hydrogen abstraction by benzophenone, a type II photoinitiator.[72]

The typical scheme for a photoinitiated free radical polymerization reactions is presented by the equations (1-4), shown below:

Eq 1.1 $PI \rightarrow PI^{*}\,(hv) \rightarrow R^{\cdot}$

Eq 1.2 $PS \rightarrow PS^{*}\,(hv) \rightarrow PI^{*} \rightarrow R^{\cdot}$

Eq 1.3 $PS \rightarrow PS^{*}\,(hv) \rightarrow PS^{\cdot +} + PI^{\cdot -} \rightarrow radicals$

Eq 1.4 $R^{\cdot} + radical\ monomer \rightarrow polymer$

1.2.1 Photopolymerization and tissue engineering scaffolds

Photopolymerization is a commonly applied approach in the synthesis of tissue engineering scaffolds, allowing for the exploitation of a readily available stimulus such as light, fast curing rates, the incorporation of non-volatile chemicals (water is used as the most common solvent)[70] and in situ gel formation.[7,73] The mild reaction conditions

of photopolymerization, allow hydrogel formation in the presence of living cells, ensuring homogeneous cell seeding across the matrix.[7] Important factors influencing cell viability in such applications are the photoinitiator type and its concentration, as well as the light intensity and wavelength.[73] Most common photoinitiator/photoinitiating systems used in biomedical applications are Irgacure 2959, Eosin, and naturally derived Riboflavin.[72]

1.2.1.1 UV light-initiated polymerization for scaffold fabrication

UV light-initiated polymerization is the most common approach employed in the preparation of cell scaffolds by photopolymerization, due to the availability of various UV light-initiators. However, the main disadvantage of UV-light polymerization lays in the cytotoxic effects of UV light that results, even when short durations are employed, in adverse effects on the metabolic activity of cells. [72]

Irgacure 2959, as well as its derivatives and in specific Irgacure 651 and Irgacure 184, constitute the most commonly used Type I UV-light photoinitiators, owing to their commercial availability. However the main disadvantage of Irgacure 2959 stems from its photoactivation only in the UV light range, as it exhibits a maximum absorption at 276 nm and a narrow absorption band limited to the UV-A range at 365 nm, which combined with its low water solubility just below 2%, translates to longer exposure times that can have unfavorable effect on the initiators' cell toxicity. [73] Other water-soluble photoinitiators have been proposed such as the commercially available Type I photoinitiator lithium phenyl-2,4,6-trimethylbenzoylphsphinate (LAP), operating in the lower visible region (405 nm), with an improved water solubility and a reduced cell cytotoxicity compared to Irgacure 2959.[74] LAP has been widely used to obtain hydrogels of PEGDA and GelMA, among other monomers.[73]

1.2.1.2 Visible light-initiated polymerization for scaffold fabrication

Visible light-initiated polymerization possesses many advantages when compared to the conventional UV initiated photopolymerization routes, mainly due to visible light being less harmful to cells and having a higher penetration depth, thus providing the ability for in situ polymerization post implantation. [72]

Visible light photopolymerization can be achieved using organic dyes as photosensitizers, such as Eosin Y in the presence of a tertiary amine acting as a cocatalyst of the initiation process (Type II initiator). Eosin Y is a water-soluble dye commonly used in histological staining, with a wide range of absorption (400 nm - 800 nm). It is compatible with living cells and has been widely used as a photoinitiator for the formation of hydrogel scaffolds (GelMA, PEGDA etc.) for cell encapsulation.[73] Riboflavin, commonly known as vitamin B2, has been also used as a naturally derived visible light photoinitiator exhibiting strong absorption in the 330 - 470 nm range. It is highly biocompatible and water soluble, and similar to Eosin Y, riboflavin is also a type II initiator which operates efficiently in the presence of a co-initiator. Additionally, low concentrations of riboflavin (0.01 – 0.5 wt%) can provide fast cross-linking rates when 10% amine is used as a cocatalyst. However, under UV or visible light irradiation and in the presence of oxygen, riboflavin can produce reactive oxygen species[75] which have been reported to be harmful for living cells[76].

The use of organic dyes as photosensitizers in visible-light photoinitiated polymerization for hydrogel scaffold fabrication in tissue engineering applications has been positively influenced by their inherent biocompatibility.[73] Their application is mainly hindered by their often low molar extinction coefficients and their narrow band absorption.[77] Variation of their efficiency, being highly dependent on the presence of a cocatalyst, renders the optimization of these systems very difficult.[77] Other disadvantages that further limit the use of both Eosin Y and Riboflavin, include their very high cost, their laborious and time consuming synthesis[78,79], and their short shelf life due to their high photosensitivity and possible photobleaching[80,81].

1.2.2 Photopolymerized gelatin scaffolds for TE applications

Gelatin methacrylamide (GelMA) is a widely used photo-cross-linkable derivative of gelatin, modified with methacrylamide groups and has been widely employed in the synthesis of hydrogel scaffolds. GelMA can be obtained by the simple reaction of gelatin with methacrylic anhydride, and the degree of functionalization can be readily tuned upon varying the molar ratio between methacrylic anhydride and the repeat units of the natural polymer.[53] Variations in the degree of functionalization of the polymer,

can result in hydrogels with different mechanical and degradation properties.[10] The introduction of photopolymerizable moieties further allows the micropatterning of GelMA using light as a stimulus, or 3D bioprinting using photopolymerizable bioinks.[21,82] Photopolymerizable GelMA hydrogels have been proposed for various tissue engineering applications.

Recently Osi et al. employed a thermo-/photo-cross-linked chitosan (ChMA)-gelatin (GelMA)-nanohydroxyapatite (nHAp) composite hydrogel bioink to obtain 3D scaffolds for bone tissue engineering using 0.25% (w/v) Irgacure 1173 as a photoinitiator, under UV light (365 nm).[12] The photo-cross-linking duration to obtain structures with high mechanical fidelity was set at 12 s. Cell viability of the bioprinted scaffolds was tested by means of cultures of bone marrow stem cells with the printed constructs and all synthesized scaffolds were proven to be nontoxic to the cells, while HAp-containing scaffolds exhibited higher viabilities than the HAp-free scaffolds on days 1 and 3 of culture. In the field of cartilage repair, Gan et al. proposed a mussel inspired dopamine-oligomer (ODMA) intercalated GelMA hydrogel, using 1 wt% Irgacure 2959 as a photoinitiator under UV irradiation (365 nm).[59] ODMA was first formed by aggregation and phenol-cross-linking of dopamine and was subsequently mixed with a GelMA solution, so that its intercalation into GelMA chains would reduce GelMA chain entanglement and improve the mechanical properties of the hydrogel. The authors reported that the resulting hydrogels could withstand twisting and bending. Chondroitin sulfate or transforming growth factor- β_3 were also incorporated in the ODMA-GelMA hydrogels and it was demonstrated that the hydrogels promoted chondrogenic differentiation of bone marrow stem cells. Arica et al. developed a GelMA-p(HEMA) hydrogel for corneal tissue engineering. They proposed a hybrid hydrogel of HEMA and electrospun GelMA fibers, using N,N methylene bis acrylamide as the cross-linker and Irgacure 2959 as the photoinitiator under UV light (365 nm) for 10 min. Hybrid hydrogel films exhibited a wavelength dependent transmittance ranging from 58% to 74% in the range of 400 nm - 800 nm, water contact angles of 40.3^{o} and a Young modulus of approximately 7 ± 1 kPa. Finally, cell viability and proliferation of corneal endothelial cells on the hybrid hydrogels showed a high

viability compared to the pure pHEMA hydrogel control and the hemolytic activity of the hydrogels was within the acceptable range.

1.3 Graphitic carbon nitride (g-C_3N_4)

Graphitic carbon nitride (g-C_3N_4) is a semiconducting carbon-based material, that has been studied and applied extensively for photocatalysis, since Wang et al.[83] first demonstrated its ability to perform water splitting under visible light irradiation in 2009. Since then, research interest in g-C_3N_4 has grown immensely and its applications have expanded from photocatalysis[83–86] to polymerization photoinitiation [87–91], bioimaging and therapy [92–95].

Bulk g-C_3N_4 can be synthesized following various simple and straightforward synthetic routes, the most common being thermal polycondensation from low molecular weight nitrogen-rich organic precursors (Fig. 1.3), such as urea, thiourea, melamine and dicyanamide at elevated temperatures (over 500 ^oC [96]). This method offers tunability of the properties of the final product by means of the precursors used [97], the duration and the temperature of polycondensation.[96]

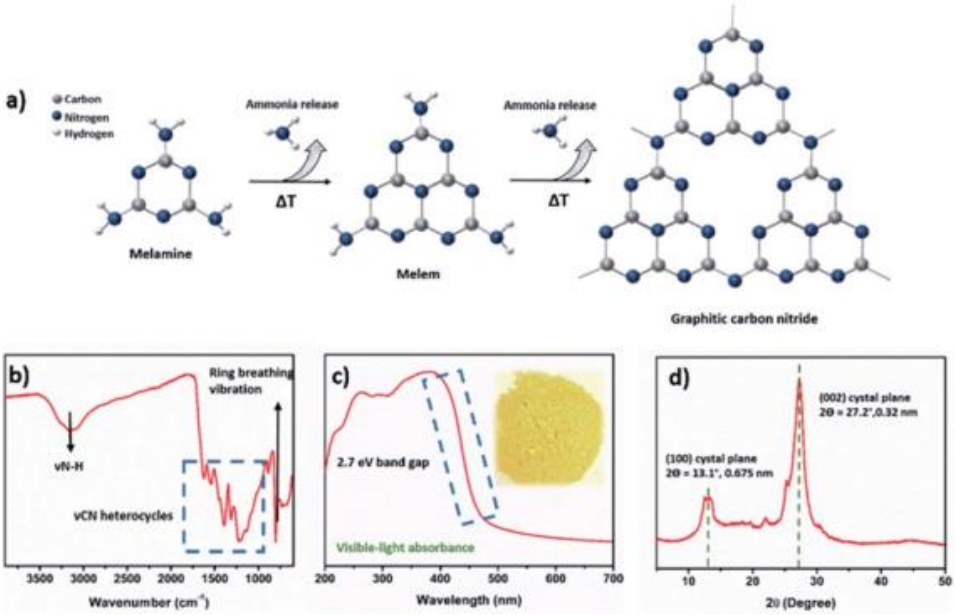

Figure 1.3 - (a) Synthetic route to obtain g-C_3N_4 from melamine. (b) FTIR and (c) UV-Vis spectra and (d) XRD pattern of g-C_3N_4.[97]

Due to the presence of nitrogen, g-C_3N_4 acts as an n-type semiconductor. Its structure is closely similar to that of graphite, with C and N atoms being sp^2 hybridized and forming a hexagonal lattice structure. The presence of nitrogen instead of carbon results in the formation of s-triazine rings and tri-s-triazine rings that are covalently linked with each other, forming two dimensional planes stacked on top of each other through π-π interactions.[98] Pristine g-C_3N_4 exhibits a 2.7 eV band gap, responsible for its visible light photocatalytic properties.[97] Under visible light irradiation of approximately 460 nm, electron-hole pairs that can readily oxidize (holes) and reduce (electrons) other molecules are generated. Unfortunately, due to the close stacking of the heptazine units in bulk g-C_3N_4, the photogenerated electrons are rapidly recombined with the holes in the lattice, resulting in a limited photocatalytic performance.[98] Several allotropes of g-C_3N_4 with superior photocatalytic properties and various dimensionalities have been reported in the literature[98], such as quantum dots[99–101] and nanosheets[84–86,92].

1.3.1 g-C_3N_4 nanosheets

g-C_3N_4 nanosheets are a 2D allotrope of g-C_3N_4, very similar to graphene, where electrons are mostly confined in the thickness direction of the nanosheets and can freely move in two dimensions. g-C_3N_4 nanosheets can be readily obtained by exfoliation of bulk g-C_3N_4 and its superior photoactivity compared to its parent precursor is assigned to the larger surface area and better optical properties.[98]

Thermal and liquid exfoliation are the most common methods used for the preparation of g-C_3N_4 nanosheets. In specific, thermal exfoliation is a facile top-down approach, where nanosheets can be obtained by weakening the Van der Waals forces between stacked layers of the bulk material.[98] Niu et al. proposed the synthesis of g-C_3N_4 nanosheets with a thickness of approximately 2 nm via a 2 h calcination of bulk g-C_3N_4 at 500 ^oC.[86] The nanosized product possessed small sheet thickness and a larger surface area. The optical properties were also improved, with the nanosheets exhibiting an increased band gap and superior photocatalytic activities under UV and visible light. Li et al. demonstrated the relationship between calcination time and nanosheet thickness

of the final product.[85] Thermal exfoliation of bulk g-C_3N_4 up to 4 h at 520 ^oC, resulted in the formation of nanosheets, while when the duration was extended to 6 h, porous ultrathin nanosheets of g-C_3N_4 bearing holes were obtained (Fig. 1.4), with exceptional photocatalytic properties.

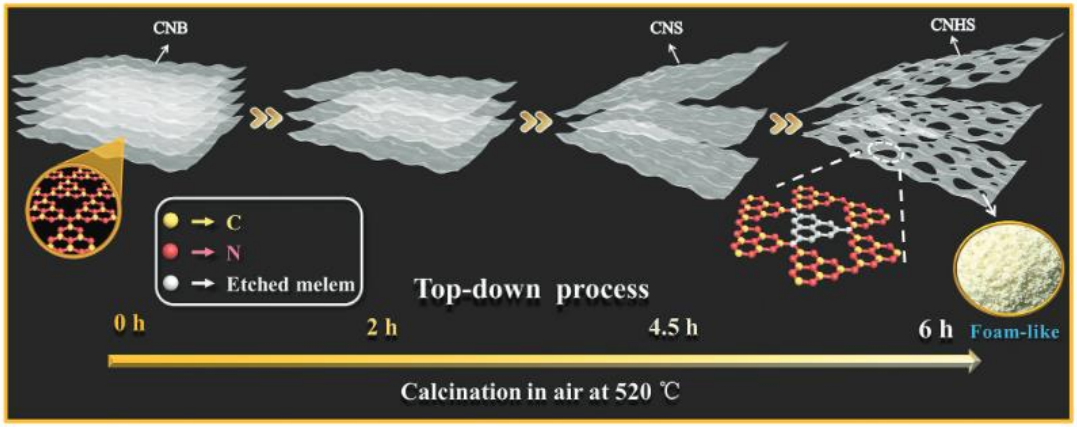

Figure 1.4 – Top-down process for the preparation of ultrathin g-C_3N_4 nanosheets from Li et al.[85]

g-C_3N_4 nanosheets can be also prepared by liquid exfoliation taking advantage of the effects of the solvent (chemical or physical) and the use of an external force such as ultrasonication, thermal energy or pressure. Xu et al. synthesized atomic single layer thin g-C_3N_4 sheets for photocatalysis by a chemical exfoliation method in H_2SO_4.[84] This was achieved by the intercalation of H_2SO_4 in the interlayer space of the bulk material and subsequent exfoliation to single layers by the addition of deionized water and sonication. However, the use of such strong chemicals can be environmentally hazardous and have negative impacts on the biocompatibility of the synthesized product. To that end, Zhang et al. proposed the preparation of 2.5 nm thick g-C_3N_4 for bioimaging via a green liquid exfoliation method in water.[92] Ultrathin g-C_3N_4 nanosheets with enhanced photoresponsivity and fluorescence for bioimaging were synthesized after 16 h sonication in water.

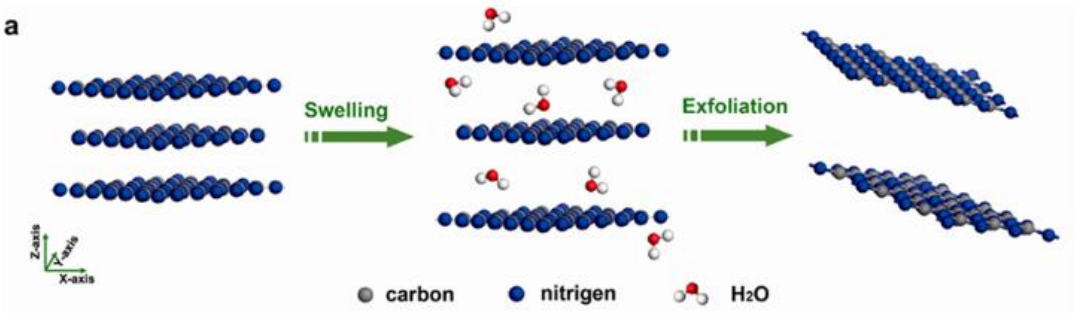

Figure 1.5 – Liquid exfoliation from bulk g-C_3N_4 to ultrathin g-C_3N_4 nanosheets from Zhang et al.[92]

1.3.2 g-C_3N_4 quantum dots (gCNQDs)

g-C_3N_4 quantum dots are a 0D allotrope of g-C_3N_4 with exceptional photo-responsive properties. gCNQDs, similar to g-C_3N_4, exhibit strong fluorescence, with a broad Stokes shift and non-overlapping emission and excitation spectra, which renders them suitable fluorescent probes for biological and environmental applications.[95,98] Various synthetic methods have been proposed in the literature for the synthesis of gCNQDs, including microwave assisted approaches, solid state synthesis and exfoliation of bulk g-C_3N_4.[98]

The solid-state synthesis of gCNQDs is the most straightforward and facile process. Patir et al. synthesized sulfur doped gCNQDs from EDTA and thiourea by heating solid mixtures of the two of different molar ratios at 150 ^oC-250 ^oC in a simple laboratory oven for 2 h.[100] The synthesized quantum dots were then immobilized onto filter paper and were evaluated for the detection of Hg^{2+} in tap water through the quenching of their fluorescence. Accordingly, Zhou et al. synthesized high quantum yield (42%) gCNQDs with tunable emission, by thermally treating solid mixtures of urea and sodium citrate at different molar ratios, at 180 ^oC in an autoclave for 1 h (Fig. 1.6).[101] The resulting gCNQDs exhibited good solubility in water and were used in cell imaging of HEK 293T cells by direct incubation.

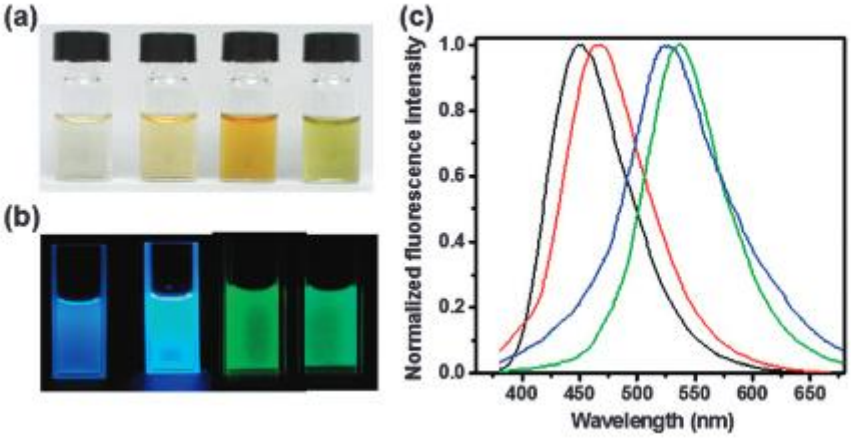

Figure 1.6 – Tunable emission of gCNQDs by tuning the molar ratio of the reactants from Zhou et al.[101] (a) Photograph of dispersions of gCNQDs synthesized by varying molar ratios of urea and sodium citrate. (b) Photo of the dispersions under UV light. (c) Fluorescence spectra of the corresponding gCNQDs.

1.3.3 g-C_3N_4 as a novel photoinitiator

As mentioned above, g-C_3N_4 allotropes have been employed in various fields of research, from environmental and energy applications to bioimaging, thanks to their desirable ability to act as highly active photocatalysts[83–86] and fluorescent probes[102–104] in the visible light range. Recently, the inherent property of g-C_3N_4 to form radicals upon visible light irradiation has been explored towards radical initiated polymerizations.[87]

Kiskan et al. first demonstrated the photoinitiating capabilities of g-C_3N_4 nanosheets using triethylamine as a cocatalyst for the photopolymerization of methyl methacrylate.[89] They proposed that in the absence of oxygen, upon light irradiation the positively charged holes formed in the semiconductor would oxidize the tertiary amine to a cation radical, which in turn would perform hydrogen abstraction from another amine to form the initiating radicals (Fig. 1.7).

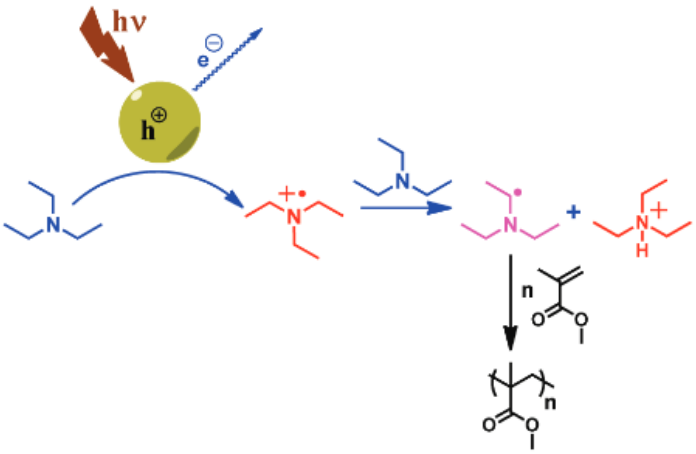

Figure 1.7 – Photoinitiation mechanism proposed by Kiskan et al.[89]

Liu et al. prepared thermo-responsive pNIPAM hydrogels using g-C_3N_4 nanosheets in the absence of a cocatalyst.[105] pNIPAM hydrogels were synthesized via photopolymerization of 10 wt% NIPAM monomer using 0.03 wt% g-C_3N_4 as the photoinitiator under an inert atmosphere. They proposed that upon light irradiation, photoexcited electrons and holes from the semiconductor could facilitate the formation of OH^- initiating radicals. They also hypothesized that the excited electrons at the conduction band had the potential to reduce O_2 to O_2^-, through the pathway $O_2 \rightarrow O_2^- \rightarrow H_2O_2 \rightarrow OH^-$ (Fig 1.8). Due to the thermo-responsive properties of pNIPAM, the obtained hydrogels exhibited thermo-responsive turbidity, where they became transparent below the lower critical solution temperature (LCST) of pNIPAM and turned opaque at elevated temperatures above the LCST. This highlighted the potential of the synthesized hydrogels to be applied in smart window applications.

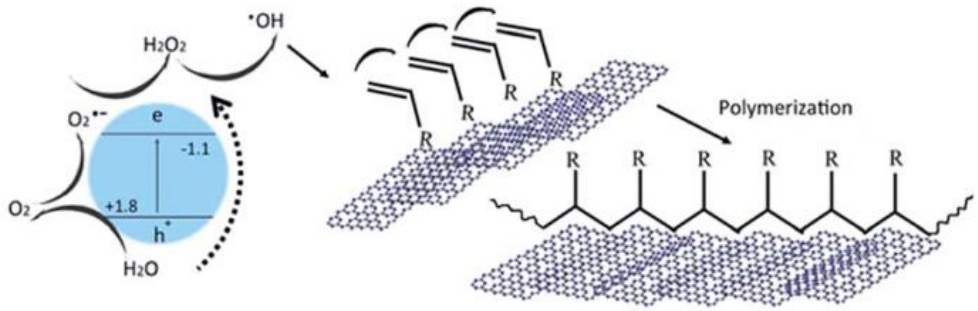

Figure 1.8 – Initiation mechanism proposed by Liu et al.[105]

Employing g-C_3N_4 nanosheets as a visible light photoinitiator, Kumru et al. demonstrated the synthesis of g-C_3N_4 photopolymerized hydrogels with extreme compressibility.[106] They suggested that g-C_3N_4 acts as a reinforcer, performing both as a photoinitiator and a cross-linker and providing an energy dissipation mechanism as a nanofiller.[90] In another paper, Kumru et al., also highlighted the beneficial combination of g-C_3N_4 with hydrophilic polymers, through visible light-induced photo-grafting of HEMA onto g-C_3N_4 to prepare well dispersed g-C_3N_4.[107] This enabled the formation of thermoset coatings via mixing the g-C_3N_4/HEMA modified precursor and citric acid as a cross-linker and the subsequent thermal treatment of the mixture. The synthesized coatings were proposed for application as photocatalytic surfaces or as photoelectrodes.

Photo-grafted polymer-carbon nitride surfaces as photocatalytic films were also proposed by Giusto et al.[108] In their paper Giusto et al. demonstrated the synthesis of polystyrene (PS)-grafted carbon nitride films with photo-switchable wettability. g-C_3N_4 thin films were prepared from melamine by chemical vapor deposition using a two-zone CVD reactor. PS photo-grafting was then conducted by coating the film surface with the vinyl monomer and its subsequent irradiation for 12 h, replenishing the monomer onto the film every 4 h. The PS coated films exhibited photo-switchable wettability that could be explained by the improved charge transfer over the surface due to the covalent grafting of the aromatic polymer onto the films and the temporary oxidation of PS.

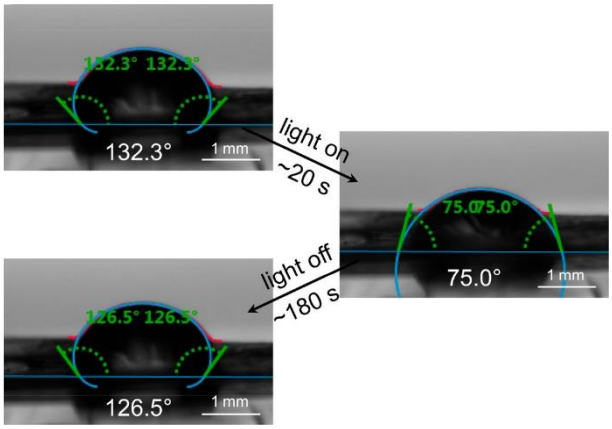

Figure 1.9 – Photo-switchable wettability of PS-carbon nitride surfaces from Giusto et al.[108]

Current applications of g-C_3N_4 as a photoinitiator are taking advantage of the photocatalytic properties of the incorporated initiator in the field of light-sensitive applications, such as the preparation of photoelectrodes and photocatalytic films. At the same time, currently biomedical applications of g-C_3N_4 are either exploiting the fluorescent properties of these materials in the fields of biosensing[95], bioimaging[101,102,109] and drug delivery[93] or taking advantage of their ability to produce radicals to induce oxidative stress in cancer therapy[110]. However, the enticing visible light photoinitiating properties of g-C_3N_4 have not been explored yet in tissue engineering applications.

1.4 Aim of this thesis

This thesis aims in the synthesis of visible-light photopolymerizable hydrogels using g-C_3N_4 as a novel photoinitiator, that will be then evaluated as scaffolds for tissue engineering applications.

To achieve this goal, photopolymerizable derivatives of dopamine and gelatin bearing methacrylate moieties were first synthesized and were employed as comonomers for the fabrication of hydrogels using g-C_3N_4 as a visible light photoinitiator. The synthesized hydrogels were fully characterized in terms of their swelling behavior, stability, and morphology and their properties were correlated to the synthetic conditions employed during their fabrication. Next, composite organic-inorganic hydrogels were synthesized by the incorporation of nanohydroxyapatite within the polymer matrix before photo-cross-linking, and the effect of the inorganic counterpart on the swelling behavior, the degradation profile and the morphology of the hydrogels was also investigated. Following an initial biocompatibility evaluation of the bare photoinitiator, an *in vitro* evaluation of the hydrogels as biomaterial scaffolds for bone tissue engineering was carried out by Mr. K. Loukelis under the supervision of Prof. M. Chatzinikolaidou, exhibiting excellent preosteoblast cell viability, as well as a high osteogenic differentiation.

Finally, preliminary results on the preparation of bioinks, via the photoinitiated cross-linking of GelMA in the presence of oxygen using methylene bisacrylamide (MBA) as

a cross-linker, g-C_3N_4 as the photoinitiator and triethanolamine as a biocompatible tertiary amine cocatalyst are presented in the final section of this thesis.

Chapter 2: g-C_3N_4 photoinitiated synthesis of hydrogels for bone tissue engineering.

2.1 Introduction

Photopolymerized hydrogels have been extensively used in biomaterial scaffolds' synthesis for 3D cell cultures.[72] Photoinitiated free radical polymerization is the polymerization strategy of choice in the field of tissue engineering due to its mild reaction conditions, being conducted at room temperature and in the presence of non-toxic and non-volatile solvents (mainly water).[7] However, most commercial photoinitiators operate under UV light, which can be toxic to cells.[72] Visible light photoinitiation is usually achieved using organic dyes as photosensitizers in the presence of tertiary amines as cocatalysts.[73] Herein, we propose the exploitation of g-C_3N_4 nanosheets, a 2D polymeric material that acts as a visible light photoinitiator, for the preparation of hydrogels based on gelatin methacrylamide and dopamine methacrylamide under an inert atmosphere. The water swelling ability and long-term stability of the hydrogels under simulated physiological conditions (in PBS, 37 ^{o}C) were readily tuned by adjusting the content of GelMA and DMA in the hydrogel precursor solution. Finally, composite hydrogels with a ~45 wt% nanohydroxyapatite (nHAp) content, that mimics the actual bone composition, as well as excellent stability (21 days *in vitro*) were obtained by the introduction of nHAp in the prepolymer solutions before photopolymerization. Finally, the *in vitro* cell response of the freeze-dried hydrogels as scaffolds for tissue engineering was investigated by the Biomaterials and Tissue Engineering Lab of the Department of Materials Science and Technology at the University of Crete (UoC), showing excellent cell viability and enhanced differentiation of preosteoblasts to mature osteoblasts, when the cells were cultured on the composite scaffolds.

2.2 Materials and Methods

2.2.1 Materials

Dopamine hydrochloride (99%) and melamine (99%) were purchased from Alfa Aesar. Methacrylic anhydride (94%), and sodium tetraborate (>99.5%), were provided by Aldrich. PBS tablets and Gelatin Type B from Bovine Skin (225g Bloom) were supplied by Sigma. Sodium hydroxide pellets were obtained from Panreac. Sodium bicarbonate (99.7%) was purchased from Sigma Aldrich. Hydroxyapatite nanoparticles (nanoXIM-Care Paste) were provided by FLUDINOVA, S.A. Hydrochloric acid was purchased from Scharlau. All solvents were supplied by Sigma Aldrich and used as received. Milli-Q water was used for the preparation of all samples and was obtained from a Millipore apparatus with a resistivity of 18.2 MΩ at 298 K.

2.2.2 Synthesis

2.2.2.1 Synthesis of the g-C_3N_4 allotropes

Bulk g-C_3N_4 was synthesized by the thermal polycondensation of melamine as proposed by Yan et al.[111] In specific, 4 g of melamine were placed in closed crucibles and were heated at 550 ^oC for 4 h, with a heating rate of 5 ^oC/min. The resulting yellow powder was repeatedly washed with milliQ water, was collected by centrifugation and dried under vacuum overnight. (1.69 g, yield ~ 42%)

Exfoliated g-C_3N_4 was prepared by the thermal exfoliation of bulk g-C_3N_4 as suggested by Niu et al.[86] For this, 3.25 g of bulk g-C_3N_4 was heated in open crucibles at 550 ^oC for 4 h, with a heating rate of 5 ^oC/min. (1.65, yield ~50%)

g-C_3N_4 nanosheets were obtained by sonicating 700 mg of the thermally exfoliated g-C_3N_4 in 70 mL milliQ water for 4 h. The milk-like dispersion was subsequently centrifuged at 3000 rpm for 10 min, the supernatant was kept while the precipitate containing larger, non-exfoliated sheets was discarded. The retrieved supernatant was centrifuged at 11000 rpm for 30 min to collect the g-C_3N_4 nanosheets and the precipitate was recovered and redispersed in 10 g of milliQ water, yielding a dispersion with a concentration of 5 mg/g.

g-C_3N_4 quantum dots (QDs) were prepared by the thermal treatment of urea as proposed by Zhou et al.[101] Briefly 3.03 g of urea and 2.43 g of sodium citrate were mixed in a mortar and then transferred in a Teflon-lined, steel autoclave and heated at 180 ^{o}C for 2h. The resulting powder was washed with ethanol and the supernatant was subsequently reduced with a rotary evaporator. The obtained QDs dispersion was diluted with milliQ water and dialyzed for 3 d using a 3.5 kDa dialysis membrane. The product was then obtained using a rotary evaporator and was dried under vacuum, yielding a brownish powder.

2.2.2.2 Synthesis of dopamine methacrylamide

For the synthesis of dopamine methacrylamide (DMA), a method proposed by P. Glass et al[112] was followed. Briefly, the reaction medium was prepared by dissolving 5 g of sodium tetraborate and 2 g of sodium bicarbonate in 50 mL of milliQ water in a three-necked spherical flask. The mixture was degassed with N_2 gas for 10 min. Afterwards, 2.5 g of dopamine hydrochloride were added under stirring, and the mixture was degassed again for a few minutes.

In a separate vial, 2.55 mL of methacrylic anhydride was dissolved in 12.5 mL of THF under stirring and the solution was subsequently degassed for 10 min. Then, the mixture was transferred into the reaction flask using a syringe. The pH of the resulting solution was maintained at pH~8 using 1 M NaOH solution and the reaction was allowed to continue overnight.

Next, the solution was washed two times with 25 mL of ethyl acetate and then filtered. The pH of the filtrate was adjusted at ~2 using a 6 M HCl solution under stirring. The organic layer of the solution was then extracted three times using 30 mL ethyl acetate. After extraction, the organic layer was dried over $MgSO_4$. The solution was filtered, precipitated in hexane, and refrigerated for 1 h to promote the formation of crystals. The supernatant was then discarded, and the precipitate was dried under vacuum overnight. The resulting DMA monomer was collected as a white crystal powder (1.96 g, yield ~ 76%).

2.2.2.3 Synthesis of gelatin methacrylate

The synthesis of gelatin methacrylate (GelMA) was performed according to a method reported by Van den Bulcke[53]. In a spherical flask, a 5 w/v% solution of gelatin in PBS was prepared under stirring at 50 ^{o}C. After the complete dissolution of gelatin to yield a clear light brown solution, methacrylic anhydride was added to the solution at different ratios, as shown in Table 2.1, targeting different degrees of functionalization. The reaction was allowed to proceed for 3 h, after which the solution was transferred to a 3.5 kDa dialysis membrane and was dialyzed against milliQ water at 40 ^{o}C for 7 d to remove any unreacted methacrylic anhydride and its byproducts. After purification, the product was freeze-dried at -85 ^{o}C (LyoQuest, Telstar) and stored at 4 ^{o}C until further use.

Table 2.1 – Reaction conditions for the synthesis of GelMA

Sample	mL of methacrylic anhydride / g of gelatin
GelMA I	0.1:1
GelMA II	0.2:1
GelMA III	0.4:1

2.2.3 Hydrogel Synthesis

2.2.3.1 GelMA-*co*-DMA hydrogels

GelMA-*co*-DMA hydrogels were synthesized employing the thermally exfoliated g-CN as the photoinitiator in the absence of an additional cross-linker. Various important experimental parameters were investigated, such as the wt% concentration of GelMA in the precursor solution and the molar ratio of DMA to the moles of the repeat unit of GelMA (Table 2.2). In all syntheses, the g-CN concentration was kept constant at 0.03 wt% and milliQ water and ethylene glycol were used as co-solvents at a 1:1 wt ratio. In the following, the GelMA-*co*-DMA hydrogels are denoted as “GxDy”, where x refers

to the wt% concentration of GelMA in the precursor solution and y to the DMA mol% ratio over the moles of repeat units of GelMA.

Table 2.2 – Reaction conditions for GelMA-*co*-DMA hydrogel synthesis

Sample	GelMA wt% in the precursor solution	DMA / repeat units of GelMA mole %	g-C_3N_4 wt%
G20	20	0	0.03
G20D20	20	20	0.03
G20D40	20	40	0.03
G10D20	10	20	0.03
G10D40	10	40	0.03

As a representative example, the synthesis of G20D20 is described below as a model synthesis for all Gel-*co*-DMA hydrogels. Briefly, 200 mg of GelMA II were dissolved in 390 mg milliQ water and 390 mg ethylene glycol in a 20 mL vial under stirring at 37 ^{o}C. After complete dissolution of the functionalized biopolymer, 16 mg of the DMA monomer were added, followed by the addition of 20 mg of a pre-sonicated 15 mg/g dispersion of the g-C_3N_4 photoinitiator. After complete mixing of all the precursors under stirring at 37 ^{o}C, the vial was sealed with a rubber septum and degassed for 10 min, followed by photopolymerization using a high intensity, white light lamp (PE175BFA Cermax® Xenon Lamp). Following the photopolymerization, the hydrogels were removed from the vials and washed with DMSO and milliQ water to remove any unreacted chemicals and subsequently freeze dried at -85 ^{o}C (LyoQuest, Telstar) and were stored at RT for further experiments Several conditions that are critical to the physicochemical characteristics of the synthesized hydrogels were

investigated, including the wt% of GelMA in the precursor solution, the degree of polymer functionalization, the mole ratio of DMA, as well as the curing time.

G20D20 hydrogels were also synthesized using g-C_3N_4 QDs as a photoinitiating system (G20D20QDs), following the protocol described above. Briefly, 200 mg of GelMA were dissolved in 300 mg milliQ water and 400 mg ethylene glycol under stirring at 37 ^oC overnight. 16 mg of DMA were also dissolved in the GelMA prepolymer solution, and afterwards 100 mg of a 3 mg/g aqueous dispersion of g-C_3N_4 QDs were mixed to yield the final precursor. The solution was degassed under a N_2 flow for 10 min and was photopolymerized using a high intensity white light lamp with emission lines in the visible and IR spectrum, fitted with an IR cut-off filter to exclude thermal polymerization effects.

2.2.3.2 GelMA-*co*-DMA/nHAp composite hydrogels

GelMA-*co*-DMA/nHAp hydrogels were synthesized using nanohydroxyapatite (nHAp) as an inorganic filler. Two different wt% ratios of nHAp to the GelMA functionalized polymer were investigated, namely 30 wt% and 50 wt%. The composite hydrogels will be denoted as “GxDyHApz” in the following, where x refers to the GelMA concentration in the precursor solution, y are the mol% DMA over the GelMA repeat units and z the HAp wt% ratio over GelMA.

The G20D20Hap50 synthesis is described as a representative example of the composite hydrogels. In a 20 ml vial, 500 mg nHAp paste (C_{Hap} = 20.7 wt%) provided by FLUDINOVA were added, along with 40 mg milliQ water and 390 mg ethylene glycol. The mixture was sonicated for 15 min before the addition of 200 mg GelMA II which was dissolved by stirring at 600 rpm and 37 ^oC, overnight. Then 16 mg DMA were added to the mixture and was left to dissolve under stirring at 37 ^oC for approximately 1 h. A g-C_3N_4 dispersion with a concentration of 15 mg/g was prepared via the sonication of 15 mg g-C_3N_4 in 500 mg milliQ water and 500 mg of ethylene glycol for 1 hr. 20 mg of this dispersion were added to the polymer-inorganic mixture and mixed by stirring for 10 min. Then, the vial was sealed with a rubber septum and the dispersion was degassed for 10 min before photopolymerization.

2.2.4 Characterization

2.2.4.1 Physicochemical and morphological characterization

Diffuse reflectance infrared spectra were recorded on a Shimadzu UV-2401 PC spectrometer equipped with an ISR-240A integrating sphere. $BaSO_4$ was used as a total reflectance standard. FTIR spectra were recorded on a Thermo Fischer Scientific Nicolet 6700 spectrometer and XRD patterns were obtained using a PANalytical Xpert Pro X-Ray diffractometer, with Cu K_α radiation (45 kV and 20 mA). The hydrogels were ground into their powder form before the XRD measurements. Composite hydrogels were also characterized by thermogravimetric analysis (TGA) (Perkin Elmer Diamond TG/DTA) under a N_2 atmosphere, over a 30 ^oC – 550 ^oC temperature range, at a heating rate of 10 ^oC/min.

^1H Nuclear Magnetic Resonance (^1H NMR) Spectra of DMA and GelMA were recorded on a Bruker AMX-500 NMR spectrometer. The DMA solution was prepared in $(CD_3)_2SO$, while the GelMA samples and their precursors were prepared in D_2O, and their spectra were recorded at 50 ^oC.

The morphology of g-C_3N_4 and of the hydrogels was observed via Field Emission Scanning Electron Microscopy (FESEM, JEOL JSM-7000F). For both bulk and exfoliated g-C_3N_4, a dilute 2-propanol dispersion of the materials was drop-casted onto a glass substrate. The substrates were left to dry overnight under ambient conditions. For the observation of the lyophilized hydrogels, a small piece was mounted on a glass substrate using carbon tape. All samples were sputtered with a Au layer before observation (10 nm for the g-C_3N_4 photoinitiator and 30 nm for the hydrogels). In addition, Energy Dispersive Spectroscopy (EDS) was employed to perform elemental analysis on the hybrid hydrogels.

2.2.4.2 Degree of swelling and degradation profiles of the hydrogels

To investigate the degrees of swelling of the hydrogels, lyophilized samples were cut into pieces and their dry mass was recorded (w_{dry}). They were next transferred in 20 mL vials filled with 5 mL PBS (pH 7.4). At predetermined time intervals, the swollen

gels were recovered from the vials, transferred onto filter paper to remove any excess of PBS, before being weighted again to obtain the corresponding $w_{swollen}$ value, and re-immersed into PBS. All measurements were conducted in RT.

The degree of swelling for each time point was calculated using equation 2.1:

$$Swelling\ Degree\ \% = \frac{w_{swollen} - w_{dry}}{w_{dry}} \times 100\% \qquad \textbf{Eq 2.1}$$

Degradation experiments were conducted by immersing the lyophilized hydrogels in 10 mL of PBS. The immersed hydrogels in medium were kept in sealed vials at 37 ^{o}C using a thermostated water bath. The swollen mass of the hydrogels was measured after 1, 7, 14 and 21 d of immersion following the same process described for the swelling measurements. The mass loss was calculated using equation 2.2., where w_{day1} is the weight of the swollen gel after 1 d and w_{dayx} is the weight of the swollen gel after x days.

$$Mass\ Loss\ \% = \frac{w_{dayx} - w_{day1}}{w_{day1}} \times 100\% \qquad \textbf{Eq 2.2}$$

All swelling and degradation studies were performed in duplicates.

2.2.5 Cell Culture Experiments

2.2.5.1 Cytocompatibility evaluation of exfoliated g-C_3N_4 and g-C_3N_4 nanosheets

The cytocompatibility assessment experiments for bulk g-C_3N_4 and g-C_3N_4 nanosheets were performed with Ms. Danai Papadogianni under the supervision of Prof. Maria Chatzinikolaidou on adherent cell lines of mouse osteoblasts (MC3T3-E1). Cell culture conditions were set at 37 ^{o}C, under a 5% CO_2 atmosphere, and the cell culture media

of choice was Minimum essential Eagle's medium (α-MEM). For the cell viability measurements, the PrestoBlue™ reagent protocol was employed.

Briefly, 5,000 cells/well were seeded in a 96-well plate overnight. Next, they were incubated with 1 μg mL^{-1}, 3.75 μg mL^{-1}, 6.25 μg mL^{-1}, 12.5 μg mL^{-1}, 25 μg mL^{-1}, 50 μg mL^{-1}, 100 μg mL^{-1}, 300 μg mL^{-1} g-C_3N_4 photoinitiator for 48 h in quadruplicates.

Afterwards, the supernatant from each well was removed and replaced with 150 μL of 1:10 Presto Blue solution in medium. The cells were incubated again under dark conditions for 1 h and the supernatant was collected and transferred to a new 96-well plate to measure the absorbance at 570 and 600 nm in a Synergy HTX Multi-Mode Microplate Reader.

2.2.5.2 *In vitro* evaluation of the hydrogels

For the *in vitro* evaluation of the synthesized hydrogels, G20D20 and G20D20HAp50 were chosen. The samples were prepared as described in the hydrogel synthesis section above and were cut into disks of 5 mm diameter and 1 mm height using a sterilized custom-made steel cutter before being placed in 96 well plates.

In preparation for the cell culture experiments, the materials were freeze-dried inside the plates, swollen again in a-MEM and freeze dried a second time, before cell seeding. Lyophilization was carried out at -40 ^{o}C, using a Telstar LyoAlpha Freeze-Drier. All cell experiments were performed by Mr. Konstantinos Loukelis under the supervision of Prof. Maria Chatzinikolaidou at the Biomaterials for Tissue Engineering Lab of the Department of Materials Science and Technology, (UoC). Cell viability was determined following the PrestoBlue™ assay protocol and experiments were carried out by seeding 25,000 MC3T3-E1 mouse osteoblast cells/well of passage 15 to 17, directly onto the freeze-dried hydrogel samples. Cell differentiation was determined by measuring alkaline phosphatase (ALP) activity and supernatant calcium concentration, while experiments were carried out by seeding 30,000 cells/well of MC3T3-E1 mouse osteoblast cell lines of passage 16 to 21, in osteogenic medium, directly onto the freeze-dried hydrogel samples.

2.3 Results and Discussion

2.3.1 Characterization of the g-C_3N_4 photoinitiators

The ATR-FTIR spectra for the bulk and exfoliated g-C_3N_4 are shown in Figure 2.1a, left. For the bulk material, characteristic peaks of the s-triazine ring modes appeared at 802 cm^{-1} and 1450 cm^{-1} alongside the C-N and C=N stretching modes at 1311 cm^{-1} and 1621 cm^{-1}, respectively[113]. In the case of the exfoliated product, the s-triazine ring modes at 804 cm^{-1} and 1452 cm^{-1} were observed, while the C-N and C=N stretching modes appeared at 1313 cm^{-1} and 1625 cm^{-1} [94]. A broad band that appeared in both spectra in the range of 3000 to 3500 cm^{-1} is representative of the vibrational modes of the -NH_2 and -NH terminal groups[86].

Structural information about the planar and interlayer stacking distances were obtained for both materials from their respective XRD patterns (Figure 2.1b). Diffraction patterns were in good agreement with the literature[96] for both the bulk and the exfoliated material and revealed two distinct peaks. Diffraction peaks at 13.24° and 13.15°, for the bulk and the exfoliated g-C_3N_4 respectively, corresponded to the planar structural stacking of the s-triazine groups with a characteristic distance d_1 approximately equal to 6.81 A. Peaks at 27.77° and 27.74° were assigned to the interlayer stacking of the lattices and correspond to an interlayer distance d_2 of 3.27 A.

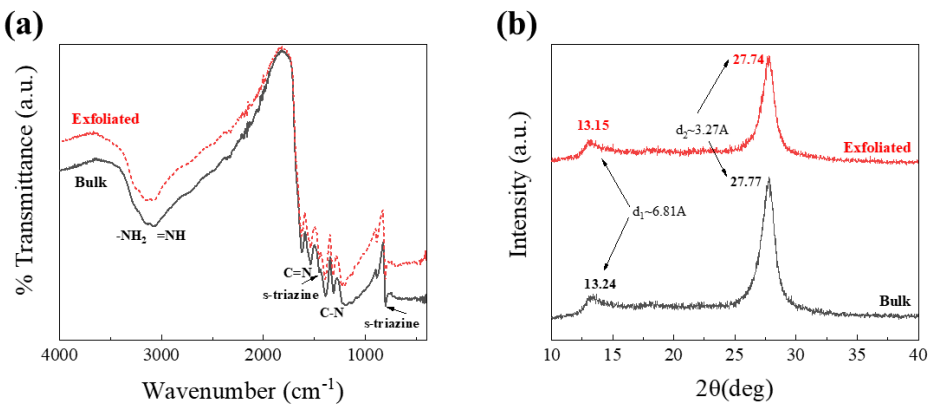

Figure 2.1 - (a) ATR FTIR spectra of bulk (black solid) and exfoliated g-C_3N_4 (red dotted). (b) XRD pattern of bulk (black) and exfoliated (red) g-C_3N_4.

The optical properties of both materials were evaluated via diffuse reflectance spectroscopy. Both bulk and exfoliated g-C_3N_4, exhibited a strong absorption in the low visible region, as can be seen in Figure 2.2. Kubelka-Munk plots derived from the DR measurements, further revealed a photonic bandgap approximately equal to 2.72 eV and a calculated excitation wavelength of 456 nm for both materials.

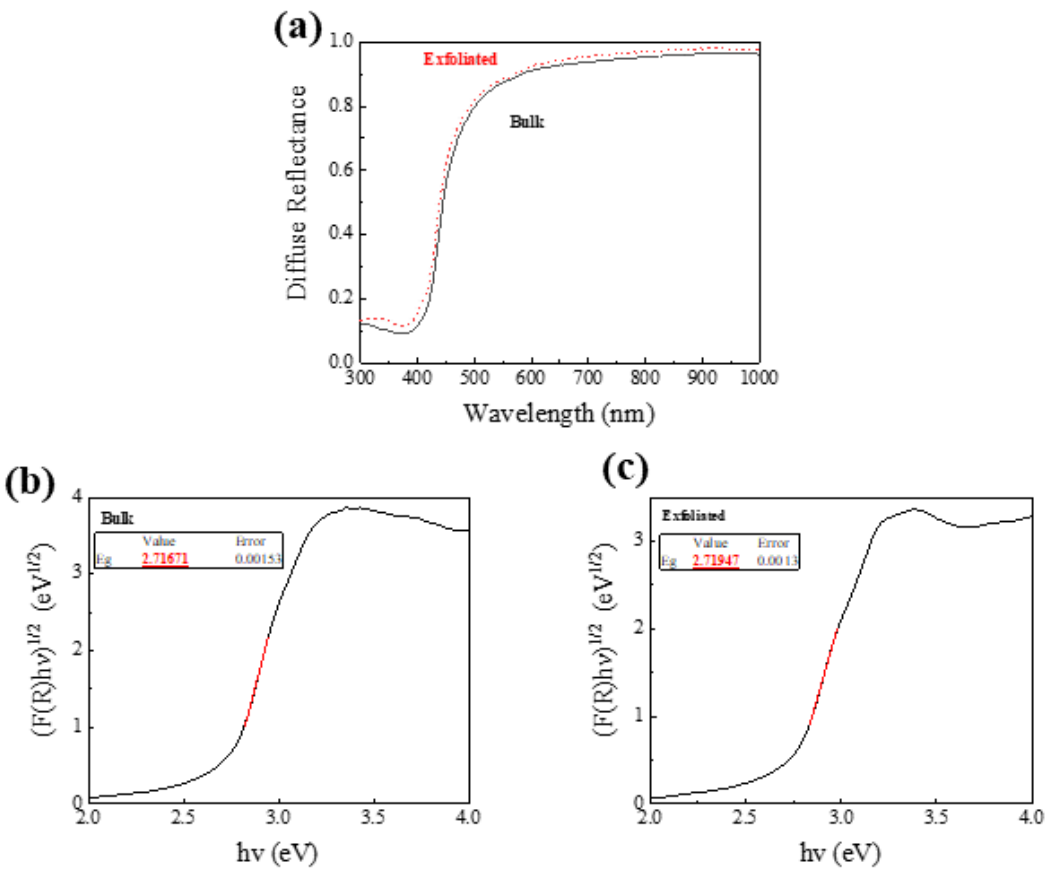

Figure 2.2- (a) DRIR spectra for bulk (black solid) and exfoliated (red dotted) g-C_3N_4. (b) Kubelka-Munk plot for bulk g-C_3N_4 and (c) Kubelka-Munk plot for exfoliated g-C_3N_4.

No significant physicochemical differences were observed between the two materials. This phenomenon could be attributed to the low exfoliation efficiency of the thermal process[114], which could be also verified by the FESEM images of the materials, as shown in Figure 2.3. Bulk g-C_3N_4 appeared to have an irregular, stacked structure. After

thermal exfoliation shear sheets covering some of the remaining crystals of the bulk material could be observed and subsequent liquid exfoliation led to the formation of nanosheets of small lateral size. Here, as reported in the literature[85,92,98], the thickness of the exfoliated materials appeared to be several times bigger than the reported interlayer distance of the stacked layers. Nanosheets of lower thickness values have also been synthesized via exfoliation routes that require the presence of strong chemicals[84], that could however have an unfavorable effect on the biocompatibility of the synthesized materials and were, thus, not appropriate for our targeted application.

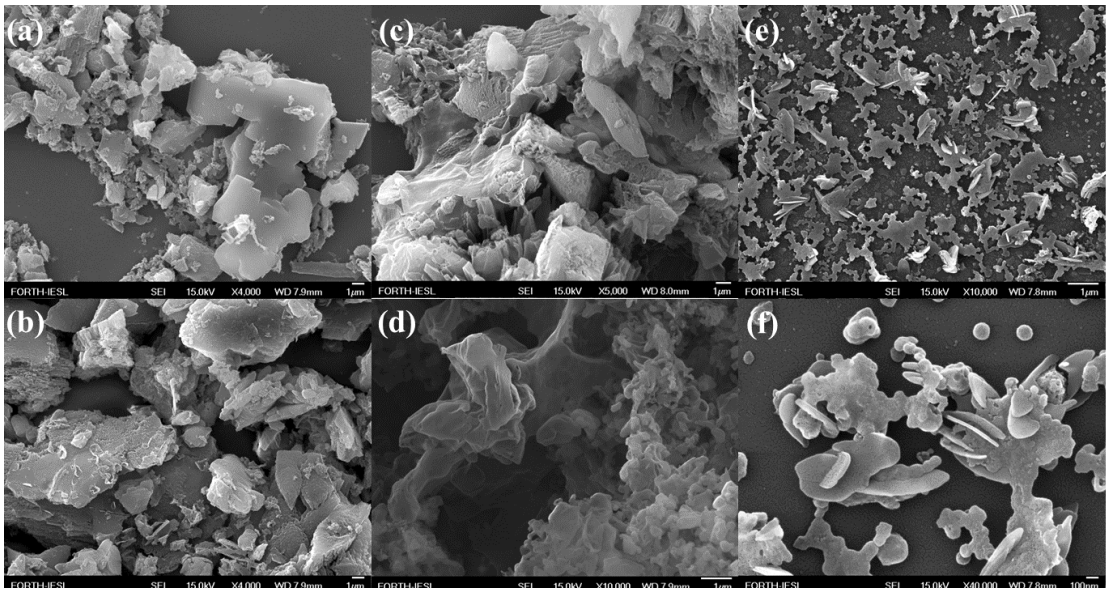

Figure 2.3 - FESEM images of g-C_3N_4. Bulk (a, b), exfoliated (c, d) and nanosheets (e,f)

Cytotoxicity assessment of both the thermally exfoliated g-C_3N_4 and the nanosheets was conducted under the supervision of Prof. M. Chatzinikolaidou and performed by Ms. Danai Papadogianni. To this end, the mouse osteoblast cell line MC3T3-E1 was incubated with different concentrations of both materials for 48 h and cell culture conditions were set at 37 ^{o}C and 5% CO_2. The w/v concentrations of the materials, as well as the duration of the experiment were planned according to similar experiments documented in the bibliography[92,93,115,116] and the concentration dependent viability of the cells over time is presented in Figure 2.4. When incubated with the thermally exfoliated g-C_3N_4, the quantified viability of the cells was found between 65% and 70% in comparison with the viability of the cells seeded on the TCPS. A 55% to 75% cell viability was observed for the cells incubated with the nanosheets. This response was

within the appropriate limits set by the ISO 10993-5-2009. Nevertheless, the slightly lower cell viability could be attributed to the precipitation of the material over the cells, also observed in the optical microscopy images taken after 48 h (Figure 2.5).

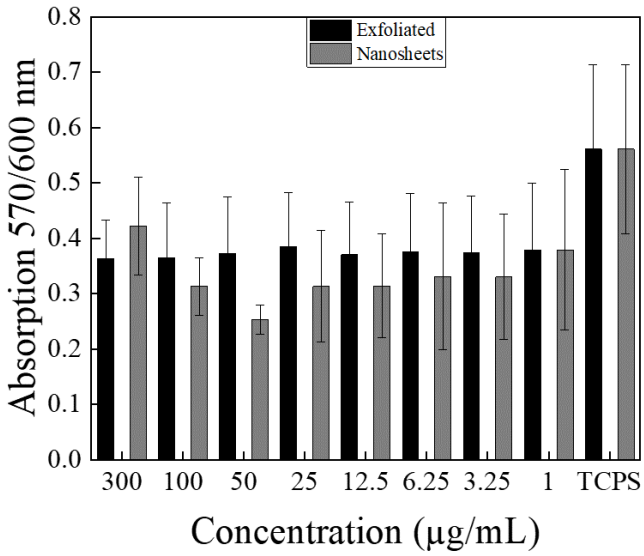

Figure 2.4 - Cytocompatibility assessment of exfoliated and g-C_3N_4 nanosheets of different concentrations measuring the metabolic activity of the MC3T3-E1 cells in absorbance units.

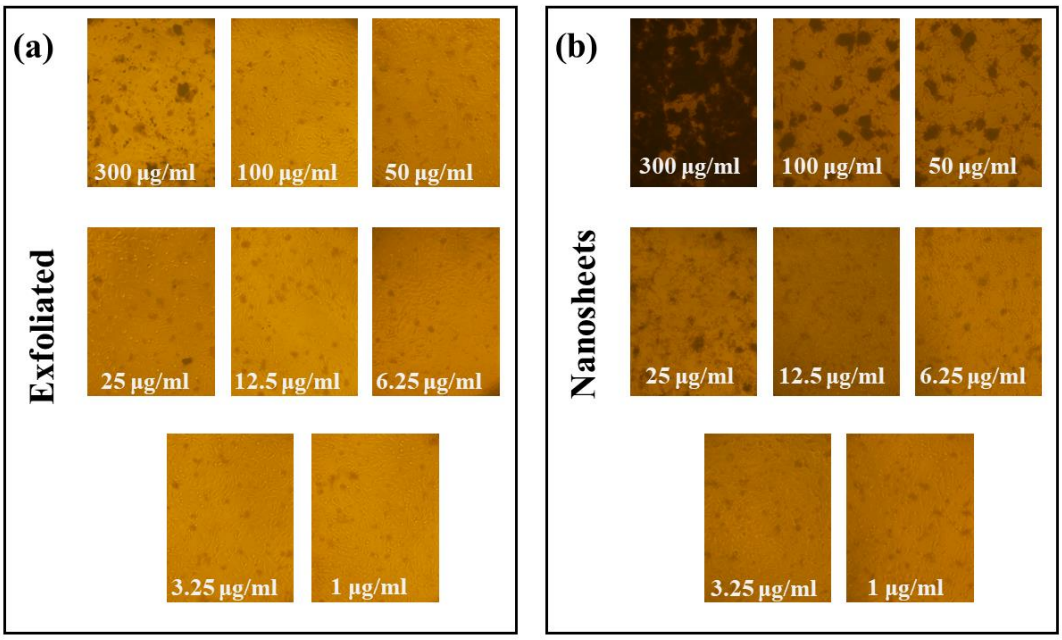

Figure 2.5 - Optical microscopy images of the thermally exfoliated g-C_3N_4 (a) and the g-C_3N_4 nanosheets (b) after 48 h cell incubation.

The thermally exfoliated g-C_3N_4 was chosen as the photoinitiator for hydrogel preparation at a concentration of 300 μg/mL (0.03 wt%), as both g-C_3N_4 nanosheets and thermally exfoliated g-C_3N_4 appear to be cytocompatible, but the synthesis of the latter proceeded at a significantly higher yield, was less time consuming, and was straightforward, involving less steps, and therefore the risk of contamination was minimized.

2.3.2 Synthesis of photopolymerizable/photo-cross-linkable derivatives from dopamine and gelatin

Photopolymerizable/photo-cross-linkable derivatives of dopamine and gelatin, named DMA and GelMA, were synthesized to bear methacrylic moieties. The successful functionalization of both dopamine and gelatin was verified by the appearance of new peaks in their respective ^{1}H NMR spectra (Figures 2.6 and 2.7), corresponding to the methylene and methyl protons of the methacrylate unit. For DMA the two characteristic peaks of the protons of the vinyl bond appeared at 5.30 ppm and 5.61 ppm, while the methyl proton peak was observed at 1.84 ppm.[117] For all methacrylated gelatin derivatives the characteristic peaks of the methylene protons appeared at approximately 5.40 ppm and 5.65 ppm, and the methyl proton peak was prominent in all spectra, at approximately 1.90 ppm.[118]

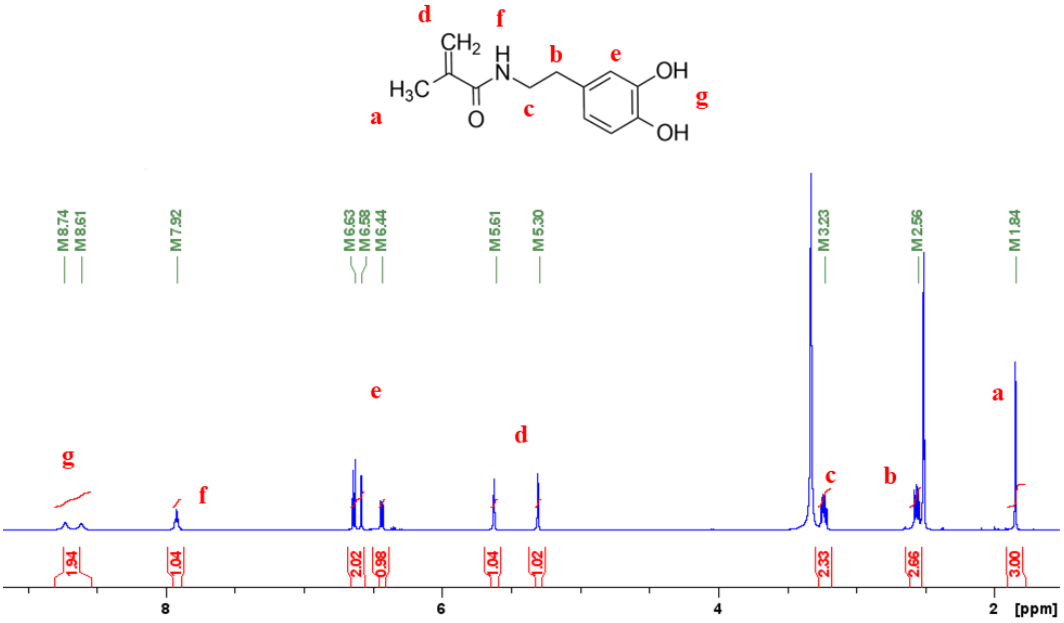

Figure 2.6 - ^{1}H NMR spectrum of dopamine methacrylamide in $(CD_3)_2SO$.

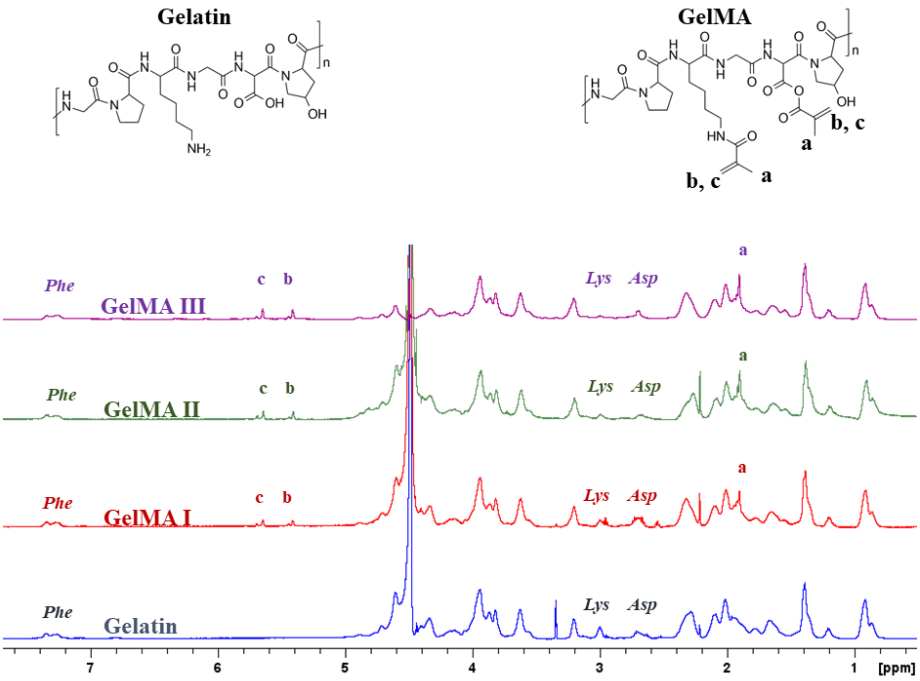

Figure 2.7 - ^{1}H NMR spectrum of gelatin and the methacrylamide derivatives at 50 ^{o}C in D_2O.

The degree of functionalization (DoF) of GelMA was calculated by comparing the integrals of the peaks of the lysine (3.00 ppm) and aspartic acid (2.72 ppm) residues to the constant integral of the phenylalanine protons at 7.3 ppm.[118] The integration results and the average degrees of functionalization are summarized in Table 2.3.

Table 2.3 – GelMA degrees of functionalization

Sample	Phe Integral (I_1)	Lys Integral (I_2)	Asp Integral (I_3)	DoF Lys	DoF Asp	Average DoF
Gelatin	5	3.58	3.98			
GelMA I	5	2.79	2.78	22.07%	30.15%	26.1%
GelMA II	5	1.86	2.59	48.04%	38.69%	43.4%
GelMA III	5	1.42	1.82	60.33 %	54.27%	57.3%

The increase in the calculated average degree of modification, that was found approximately 26%, 43% and 57% for GelMA I, GelMA II and GelMA III respectively, was expected as a result of the increase of the ratio of methacrylic anhydride to gelatin used in the feed ratio of the reactions.

2.3.3 Preparation of the GelMA-*co*-DMA hydrogels and optimization of the reaction conditions

To determine the optimum GelMA-*co*-DMA hydrogel formulation using thermally exfoliated g-C_3N_4 as a photoinitiator for the *in vitro* cell studies, various synthetic parameters that were expected to affect critical hydrogel characteristics were first evaluated. In specific, the effect of GelMA concentration (10 wt% and 20 wt%) in the precursor solution, as well as the molar ratio of the DMA comonomer to GelMA were studied. Moreover, the influence of the irradiation time of the precursor solutions was

also investigated. Last but not least, the effect of the degree of functionalization of the GelMA prepolymer was also investigated for the hydrogel with 10 wt% GelMA concentration in solution. The concentration of the g-C_3N_4 photoinitiator was kept constant at 0.03 wt% for all hydrogel formulations, based on the *in vitro* biocompatibility results of the photoinitiator, while the inverted vial method was used to confirm gel formation. The reaction conditions are summarized in Table 2.4.

Table 2.4 – Reaction conditions: degree of functionalization of GelMA and irradiation time

Sample*	GelMA wt%	DMA mole %	GelMA DoF	Irradiation Time
G20	20	0	43%	6h
G20D20	20	20	43%	6h
G20D40	20	40	43%	6h
G20D403h	20	40	43%	3h
G10D20	10	20	43%	6h
G10D40	10	40	43%	6h
G10D20F60	10	20	57%	6h

*g-C_3N_4: 0.03 wt%

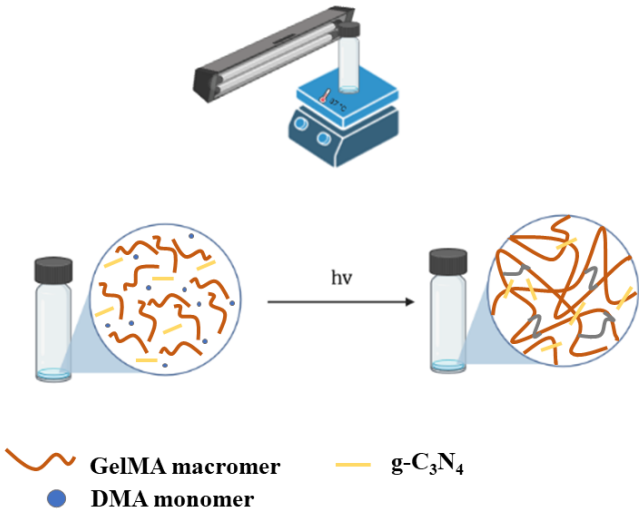

Figure 2.8 - Schematic representation of the experimental setup used for the preparation of the hydrogels.

2.3.3.1 Degrees of swelling and degradation profiles for the GelMA-*co*-DMA hydrogels

The swelling properties of the hydrogels in water are directly related to the hydrophilicity of the constructs and their relative cross-linking density.[119] Water absorption capacity is crucial to the performance of the hydrogel, influencing its physical properties and its structural and mechanical fidelity.[12] While higher degrees of swelling would favor permeability of water soluble metabolites and transport of nutrients[120], lower degrees of swelling are associated with improved matrix stiffness[12].

The effect of GelMA concentration in the precursor solution and the molar ratio of DMA over the moles of the repeat unit of GelMA on the degree of swelling of the hydrogels, along with the degradation profiles of the synthesized hydrogels were investigated. The degree of swelling was found to depend on both factors, as expected. Higher concentrations of GelMA in the precursor solution resulted in lower degrees of swelling (Figure 2.9), as was previously reported in the literature[10]. The concentration of the DMA comonomer had a similar effect on the degree of swelling of the hydrogels, which was attributed to the ability of the catechol moieties to self-cross-link via π-π stacking, hydrogen bonding, etc.[58] We have to highlight though, that the degree of swelling of G20, yielding an average maximum swelling of 570%, was found comparable to that observed for G20D20 at 540%. This was correlated with the very low concentration of DMA (0.016 wt%) in the precursor solution of G20D20, when compared to GelMA (0.2 wt%), and highlighted the role of the methacrylamide moieties of GelMA as the main cross-linking mechanism in the formation of the polymer networks. These observations were also supported by the degradation profiles of the hydrogels. Lower concentrations of GelMA in the precursor solution resulted in less stable hydrogels that exhibited a relatively fast degradation profile, reaching an average of almost 50% remaining mass after 14 d in PBS at 37 ^{o}C, in the absence of catalytic enzymes. What is more, while the differences between the degradation profiles of G20, G20D20 and G20D40 in the first 7 d were negligible, after 21 d G20 exhibited an average mass loss of approximately 10%, which further strengthened the hypothesis of catechol self-cross-linking as a supportive cross-linking mechanism, awarding the hydrogels with prolonged stability at least for 3 weeks in PBS.

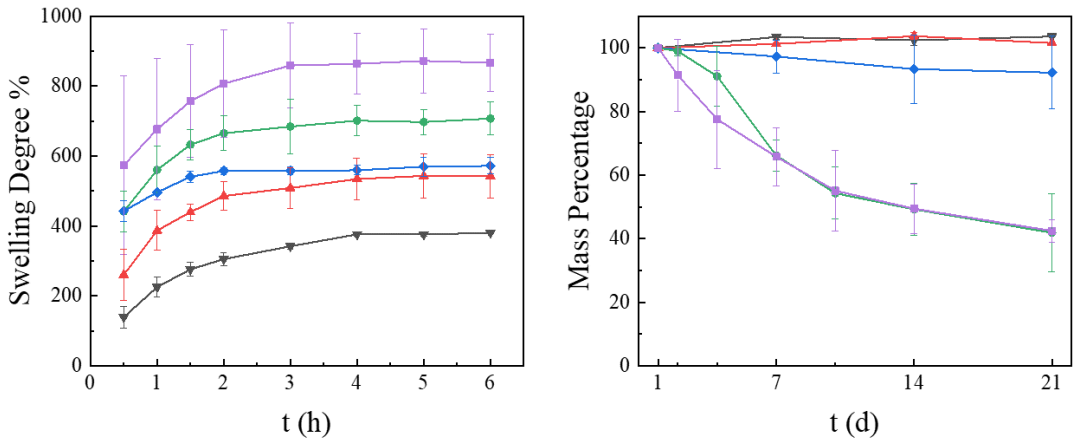

Figure 2.9 - Degrees of swelling (left) and degradation profiles (right) over time for the G10D20 (purple ■), G10D40 (green ●), G20 (blue ◆), G20D20 (red ▲) and G20D40 (black ▼) hydrogels.

A higher degree of GelMA functionalization (~56%), to enhance the stability of the prepared hydrogels, was then investigated for the G10D20 hydrogel which exhibited the lowest stability in PBS at 37 ºC and a 20% mass loss over 4 d, as described above. A higher degree of GelMA functionalization improved the physical properties of the hydrogel (G10D20F60), which maintained ~97% of its mass after 21 d in PBS at 37 ºC (Figure 2.10), in good agreement with the literature[10,55]. This could be attributed to the increase in the cross-linking density, also evidenced by the lower degree of swelling observed for G10D20F60 (750%), when compared to G10D20 (870%), due to the presence of a larger number of poly-cross-linkable moieties on GelMA.

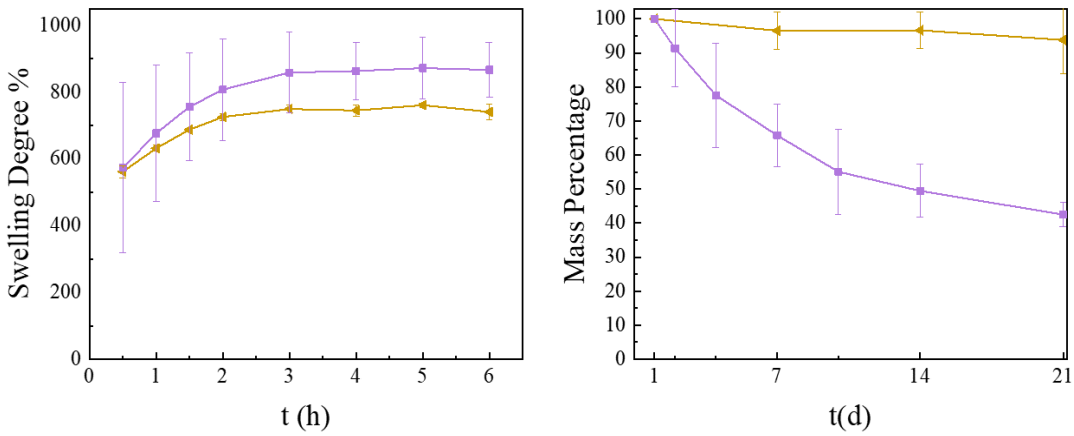

Figure 2.10 - Degrees of swelling (left) and degradation profiles (right) over time for the G10D20 (purple ■) and G10D20F60 (yellow ◀) hydrogels.

Next, the effect of irradiation time for G20D40 was investigated, the hydrogel that exhibited the highest cross-linking density as described above, and the respective swelling and degradation profiles are shown in Figure 2.11. Based on the swelling profile of the hydrogel, a shorter illumination time resulted in a less dense polymer network since G20D403h exhibited higher degrees of swelling compared to those for G20D40. In good agreement with the degree of swelling, lower hydrogel stability was found for the hydrogel synthesized at shorter photoirradiation times, with G20D40 retaining its full mass over 21 d, while G20D403h exhibits a mass loss of 30% in just 14 d and a remaining mass of ~60% after 3 weeks. The above verify our hypothesis on the effect of irradiation time on the cross-linking density and stability of the hydrogels.

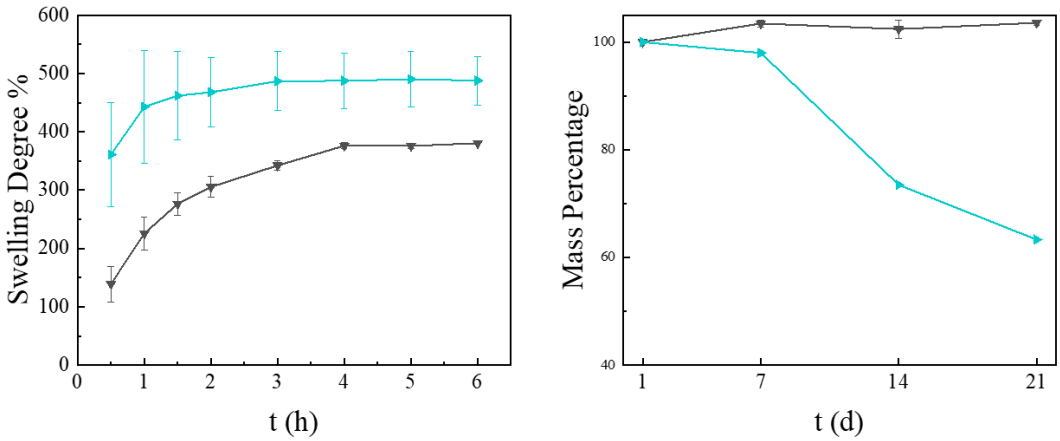

Figure 2.11 - Degrees of swelling (left) and degradation profiles (right) over time for the G20D40 (black ▼) and G20D403h (bright blue ▶) hydrogels.

2.3.3.2 Morphology of the GelMA-*co*-DMA hydrogels

The morphology and porosity of the materials that will serve as scaffolds in tissue engineering applications are of crucial importance as they can play an important role in determining the cell fate.[121] Towards this direction a high porosity and pore interconnectivity can be beneficial for nutrient diffusion and oxygen permeation[122]. The SEM images of the freeze-dried GelMA-*co*-DMA hydrogels, are presented in Figure 2.12 and revealed highly porous structures with well-defined interconnected pores. The

pore size distributions, presented in Figure 2.13 for all hydrogels, were obtained by measuring at least 200 pores using the ImageJ image processing software. The results were in agreement with our observations on the cross-link density of the hydrogels based on the swelling profiles of the respective samples (Figure 2.11(a)). More specifically, the hydrogels that exhibited higher degrees of swelling were characterized by higher average pore sizes, associated with a less dense porous network[119].

The pore size of the hydrogel appeared to be regulated by the concentration of both GelMA and DMA in the precursor solution. As it could be observed for both lower and higher concentrations of GelMA (Fig. 2.12 (a), (b), (d), (e), (f) and Fig 2.13 (a), (b), (d), (e), (f)), increasing the concentration of DMA in the prepolymer solution resulted in lower pore size and the formation of a denser porous mesh, further indicating the role of catechol self-cross-linking in gel formation. While for G10D20, the pore size distribution was centered around ~13 μm, the mean pore size for G10D40 was almost half at approximately 6 μm. Similar was observed for the mean pore size of G20D20 (~8 μm) and G20D40 (~4 μm). On the other hand, varying GelMA concentration in the precursor solution had a similar effect. There was an apparent increase in wall thickness with the formation of pores of smaller size for higher concentrations of GelMA in the precursor solution. However, the pore size distributions of G20 and G20D20 did not reveal significant differences as they were both centered around ~8 μm.

The degree of functionalization of the GelMA prepolymer had also a significant effect on the pore size of the hydrogels (Fig. 2.12 (a), (c) and Fig. 2.13 (a), (c)). While G10D20F60 had a large porous structure with pore sizes ranging from 4 μm to 14 μm, it exhibited a mean pore size of approximately 8 μm which was significantly lower than that of G10D20 (~13 μm). This was expected since the higher degree of functionalization of GelMA contributes to a higher cross-link density of the hydrogels[10,55].

In terms of the irradiation time, shorter exposure times had an effect on the morphology and the mean pore size of the obtained hydrogels (Fig. 2.12 (f), (g) and Fig. 2.13 (f), (g)). The mean pore size for G20D403h (~8 μm) is almost double that of G20D40 (~4 μm), signifying the lower cross-link density achieved when shorter exposure times are

used and providing further support to the higher degree of swelling observed for G20D203h.

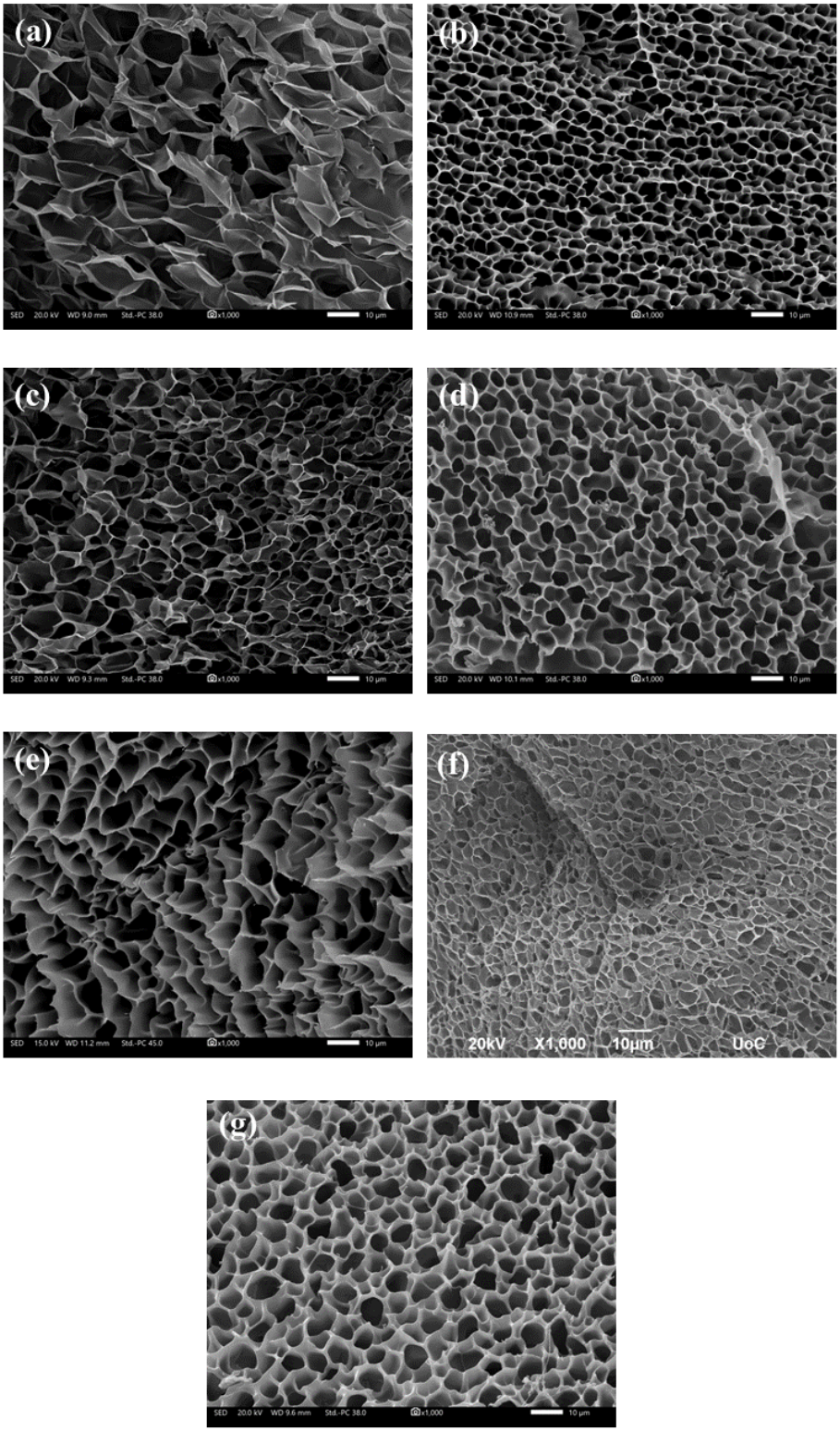

Figure 2.12 - SEM images of the freeze-dried GelMA-*co*-DMA hydrogels. (a) G10D20, (b) G10D40, (c) G10D20F60, (d) G20, (e) G20D20, (f) G20D40 and (g) G20D403h hydrogels.

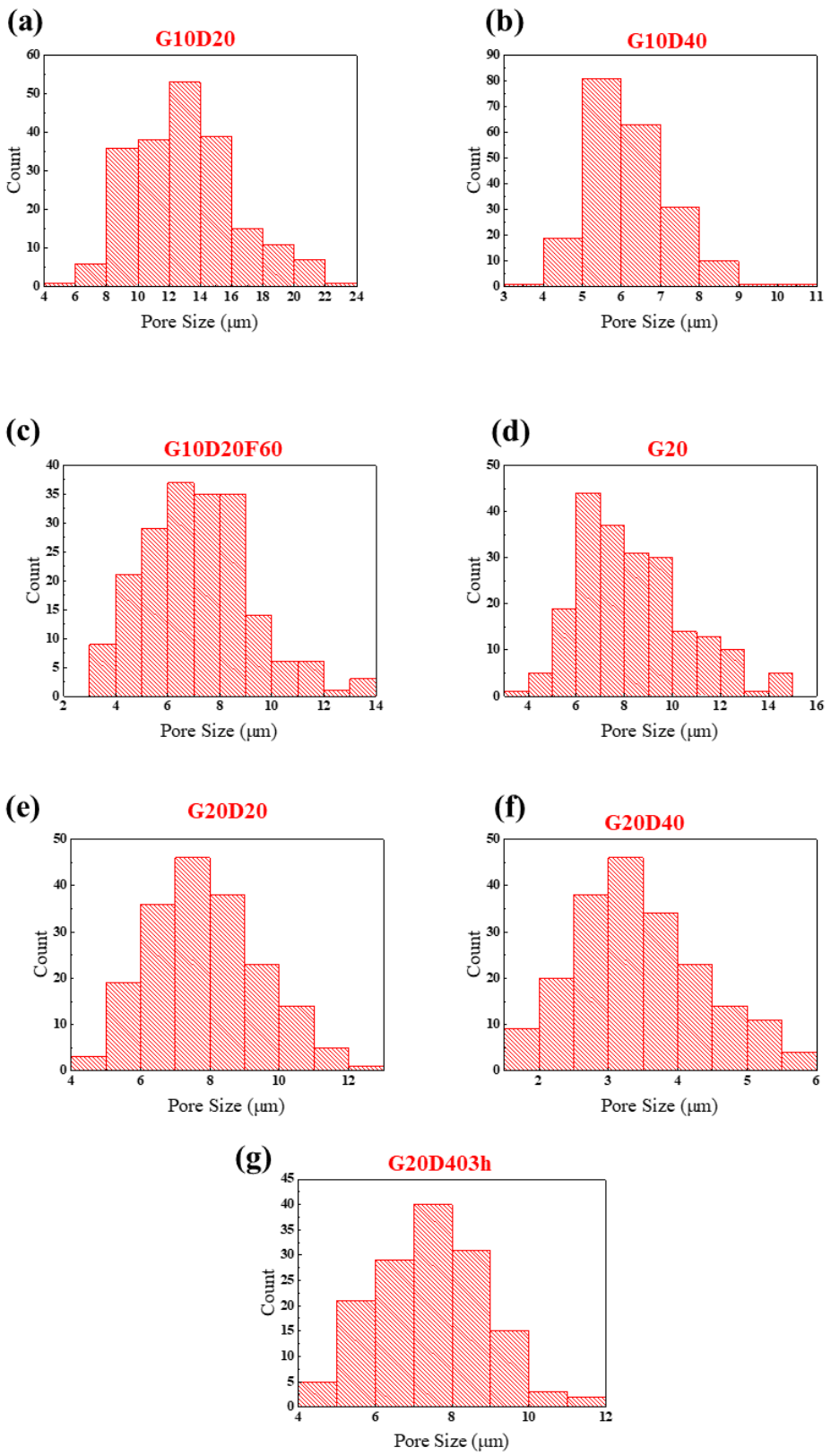

Figure 2.13 - Pore size distributions of the freeze-dried GelMA-*co*-DMA hydrogels obtained from the SEM images. (a) G10D20, (b) G10D40, (c) G10D20F60, (d) G20, (e) G20D20, (f) G20D40 and (g) G20D403h hydrogels.

2.3.4 GelMA-*co*-DMA/nHAp composite hydrogels

Based on the results discussed above for the GelMA-*co*-DMA hydrogels, the experimental conditions employed for the synthesis of G20D20 were adopted in the synthesis of composite hydrogels containing nHAp. The reaction conditions employed for these syntheses are summarized in Table 2.5.

Table 2.5 – Composition of the GelMA-*co*-DMA/nHAp hydrogels

Sample*	GelMA wt%	DMA mole %	nHAp wt%
G20D20	20	20	0
G20D20HAp30	20	20	30
G20D20HAp50	20	20	50

*g-C_3N_4: 0.03 wt%, GelMA DoF: 43%, irradiation time 6 h

2.3.4.1 Physicochemical characterization of the composite hydrogels

The successful incorporation of nHAp and its presence in the composite GelMA-*co*-DMA/nHAp hydrogels was verified by FTIR spectroscopy and XRD measurements (Figure 2.14). The characteristic peaks of GelMA appeared in the ATR FTIR spectra of both G20D20 and G20D20HApx, where x represents the weight fraction of nHAp in the hydrogels, 30 and 50 wt% in this work. More specifically, the O-H and N-H stretching vibrations of the natural polymer appeared in the 3000 cm^{-1} - 3600 cm^{-1} range in both spectra. The characteristic stretching vibration modes of amide I (C=O), amide II (N-H) and amide III (in the plane of C-N and N-H) were also observed for all hydrogels at approximately 1629 cm^{-1}, 1531 cm^{-1} and 1234 cm^{-1}, respectively. Moreover, the peaks at 2940 cm^{-1} and 1442 cm^{-1} can be assigned to the stretching and deformation modes of C-H. The presence of nHAp in the composite hydrogels is confirmed by the emergence of new sharp peaks at 1091 cm^{-1}, 1028 cm^{-1} and 962 cm^{-1}, and at 1089 cm^{-1}, 1029 cm^{-1} and 962 cm^{-1}, corresponding to the (ν3) vibrational

modes of PO_4^{3-} and at 628 cm^{-1}, 599 cm^{-1}, 559 cm^{-1} and 628 cm^{-1}, 599 cm^{-1} 561 cm^{-1} for the (ν4) vibrational modes of PO_4^{3-} in the spectra of G20D20HAp30 and G20D20HAp50, respectively. The peaks corresponding to nHAp become more intense compared to the polymer peaks in the spectrum of G20D20HAp50 signifying the higher concentration of the inorganic filler in this sample.

The XRD pattern of bare nHAp (Figure 2.14) exhibited characteristics peaks of the hydroxyapatite crystallographic planes (002), (211), (300), (202), (310) , (222), (312) and (213) at 2θ 26°, 31.9°, 32.9°, 34.2°, 39.8°, 46.7°, 48.3° and 49.6°, respectively[123,124]. These characteristic peaks were also detected in the XRD patterns of G20D20HAp30 and G20D20HAp50, while their intensity became more pronounced when increasing the HAp content of the sample.

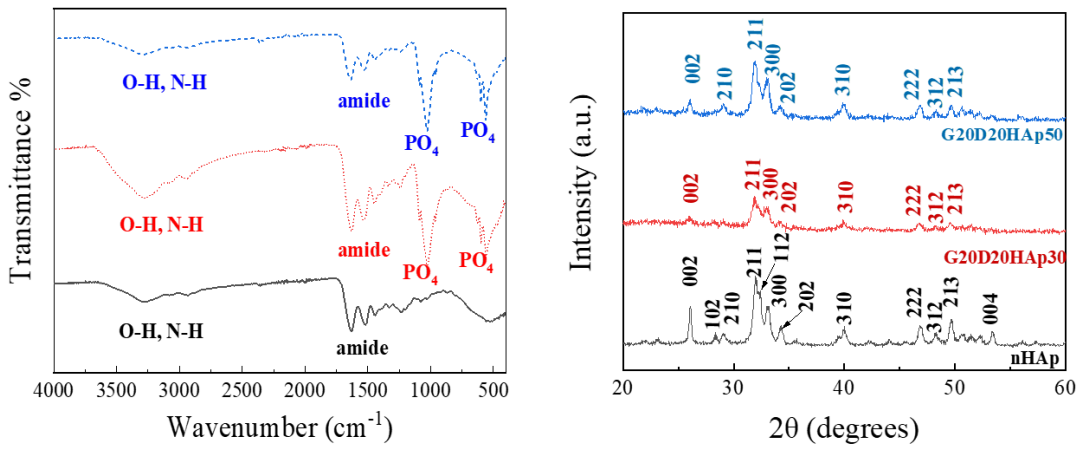

Figure 2.14 - FTIR spectra (left) of the G20D20 (black solid), G20D20HAp30 (red dotted) and G20D20HAp50 (blue dashed) hydrogels and XRD patterns (right) of nHAp (black) and the G20D20HAp30 (red) and G20D20HAp50 (blue) hydrogels.

The nHAp nanoparticles and the composite hydrogels were further characterized by TGA (Figure 2.15) to quantify the nHAp mass incorporated in the final hydrogels after their purification via repeated washing with fresh solvent. For the bare nHAp nanorods (Figure 2.15, inset), a small weight loss of approximately 3% was observed up to 500 °C, which was attributed to the carbonate groups formed due to CO_2 adsorption on the surface of the apatite[125]. For the G20D20 hydrogel, a gradual weight loss was observed when increasing the temperature up to 500 °C, and a remaining weight fraction of 28%,

which is in good agreement with previously recorded thermogravimetric analysis of GelMA[11], was found. For, the composite hydrogels, lower weight losses were observed in comparison to the bare polymer hydrogel (G20D20). In addition, the observed remaining weight was found dependent on the nHAp concentration, at 52% and 60% for G20D20HAp30 and G20D20HAp50, respectively. Considering the incomplete thermal degradation of the G20D20 hydrogel, the respective inorganic content for the G20D20HAp30 and G20D20HAp50 hydrogels, was found approximately equal to 29.7% and 44.9%, verifying the successful and quantitative incorporation of nHAp in the G20D20 hydrogels. This high percentage of nHAp incorporation, even after extensive washing of the hydrogels, may be attributed to the presence of the catechol groups and their high binding affinity for Ca^{2+} leading to the strong anchoring of the inorganic nanoparticles within the polymer matrix[59,68].

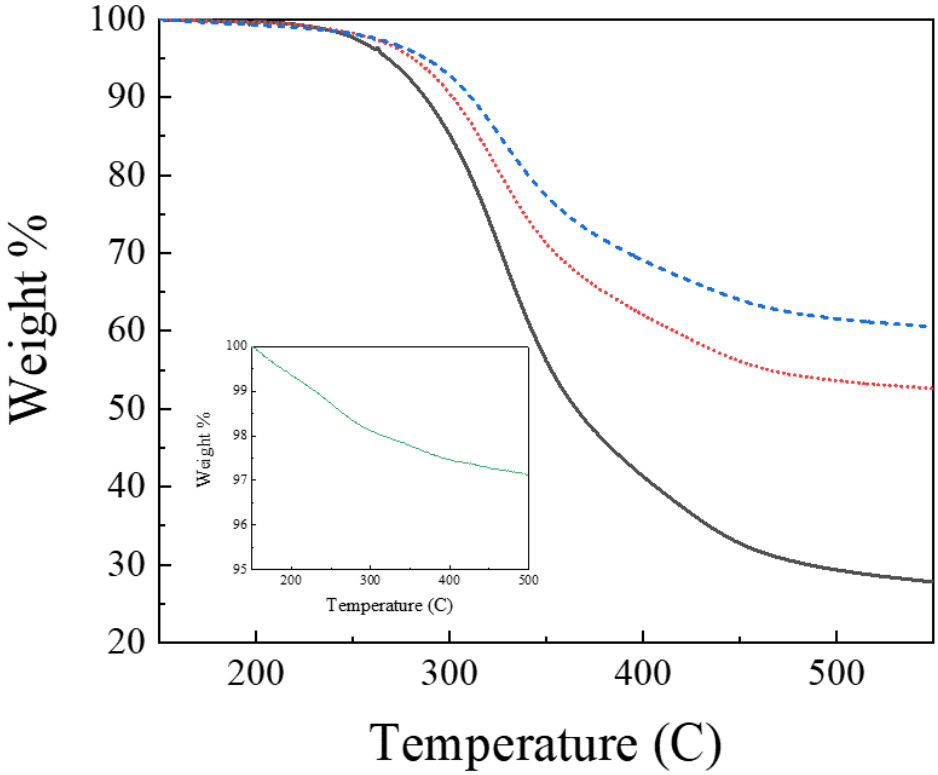

Figure 2.15 - TGA curves for the G20D20 (black solid), G20D20HAp30 (red dotted) and G20D20HAp50 (blue dashed) hydrogels. Embedded is the TGA curve for nHAp (green).

2.3.4.2 Swelling and degradation profiles of the composite hydrogels

The effect of nHAp on the swelling behavior of the composite hydrogels is presented in Fig. 3.14. It is clear that the incorporation of nHAp reduced the maximum degree of swelling of the composite hydrogels compared to the polymer analogues, in agreement with what has been previously reported in the literature[12,13]. This behavior was also found to depend on the concentration of the inorganic component, since when increasing the HAp content, the maximum degree of swelling decreased to 370% and 270% for G20D20HAp30 and G20D20HAp50, respectively, in comparison to the 540% degree of swelling for the bare G20D20 hydrogel. This was attributed to the further anchoring of the polymer chains on the inorganic surface discussed above, as well as the reduced mobility of the polymer chains in the presence of nHAp due to steric hindrance[23].

The incorporation of nHAp in the composite hydrogels was not found to impose any significant effect on the stability of the hydrogels in PBS, as illustrated in the degradation profiles depicted in Fig. 2.16. Both the bare, G20D20, and the composite, G20D20HAp30 and G20D20HAp50, hydrogels retained ~100% of their total mass for at least 21 d in PBS.

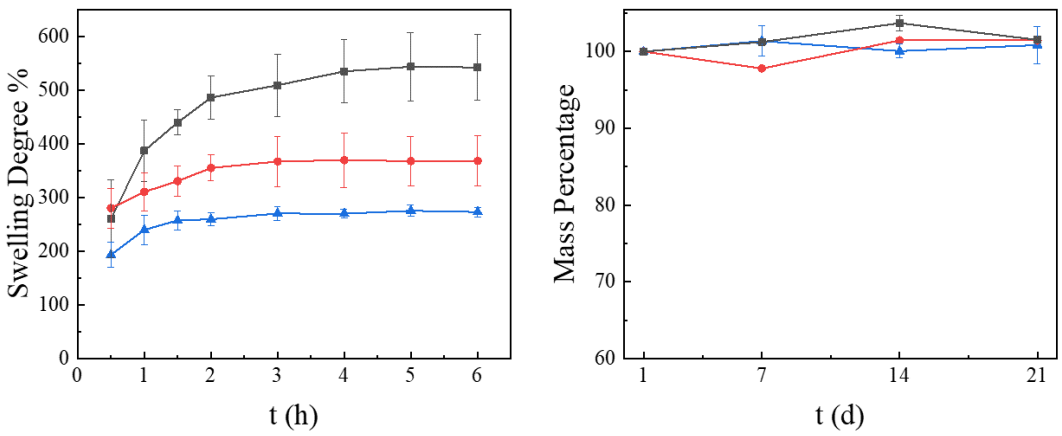

Figure 2.16 - Degrees of swelling (left) and degradation profiles (right) over time for the composite hydrogels. G20D20 (black ■), G20D20HAp30 (red ●) and G20D20HAp50 (blue ▲) hydrogels.

2.3.4.3 Morphology of the composite hydrogels

The SEM images and EDS results of the freeze-dried composite hydrogels are shown in Figures 2.17 -2.19, revealing the porous morphology of the composite hydrogels,

and verifying the presence of Hap, via the appearance of the Ca and P signals. The presence of HAp led to the formation of larger pores and more irregular porous meshes. This effect became more prominent for the G20D20HAp50 sample and was attributed to the structural heterogeneity introduced by the nHAp aggregates in good agreement with the literature[23]. More defects appeared on the pore walls of the composite hydrogels, as well as a rougher surface due to presence of the rod-like nanoparticles.

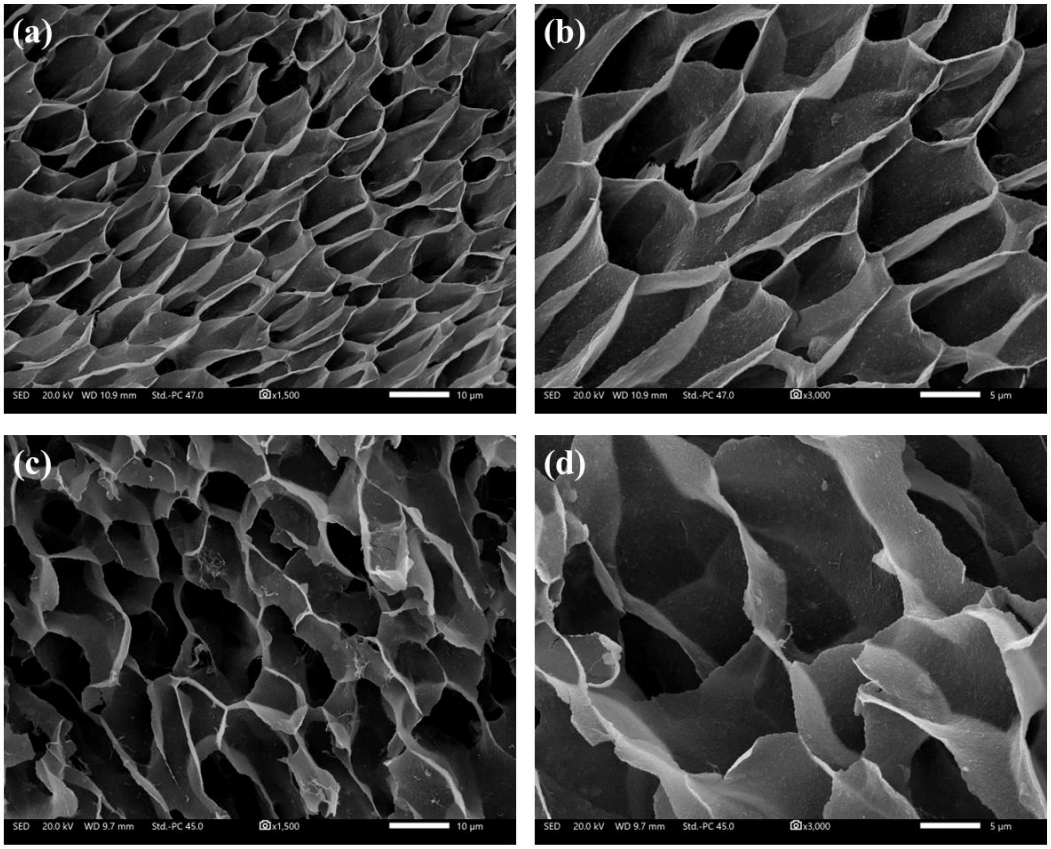

Figure 2.17 - SEM images of the freeze-dried G20D20HAp30 (a), (b) and G20D20HAp50 (c), (d) hydrogels.

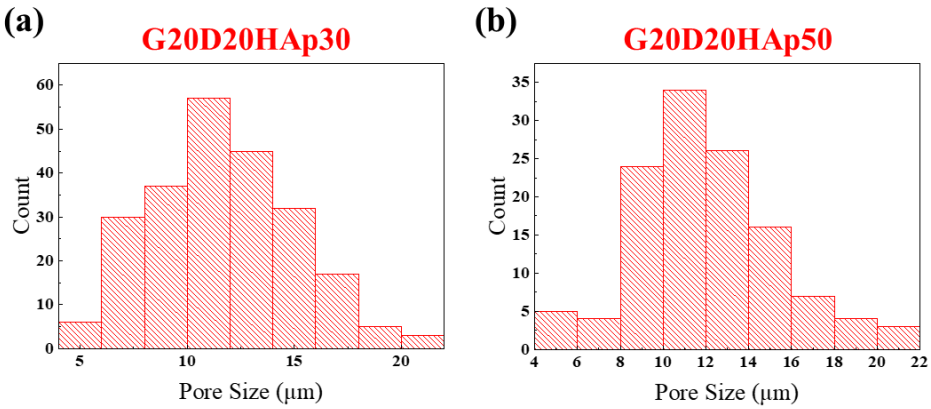

Figure 2.18 - Pore size distributions for the G20D20HAp30 (a) and G20D20HAp50 (b) hydrogels determined from the SEM images.

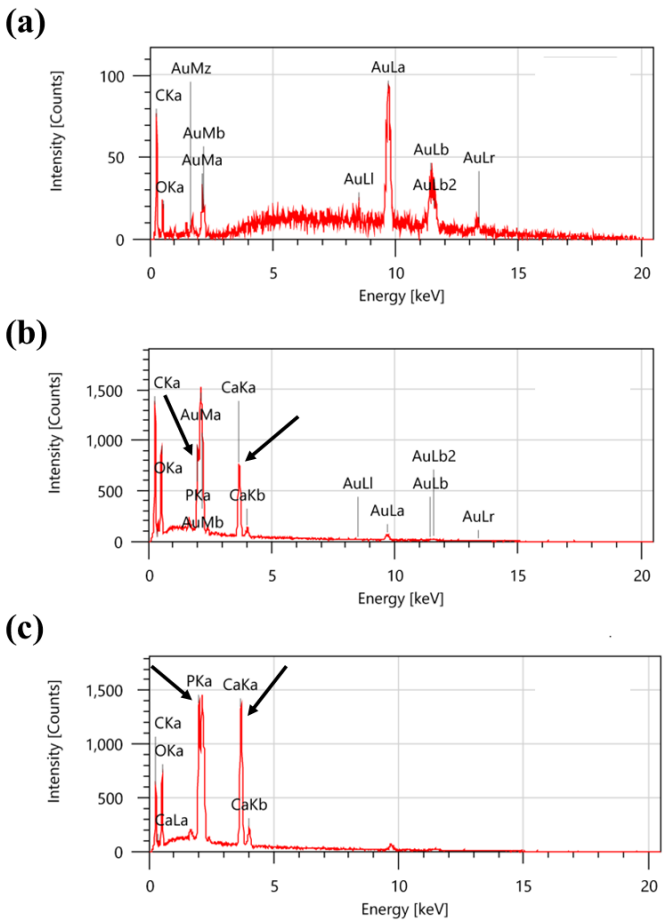

Figure 2.19 - EDS spectra of the (a) G20D20, (b) G20D20HAp30 and (c) G20D20HAp50 hydrogels.

For the *in-vitro* cell culture experiments, the G20D20HAp50 hydrogel was chosen due to its biomimetic approach to simulate the high nHAp content of native bone (~60%)[126].

2.3.4.4 *In vitro* cellular response of the composite hydrogels

Experiments on the *in-vitro* cellular response of the G20D20 and G20D20HAp50 hydrogels were carried out under the supervision of Prof. Maria Chatzinikolaidou by Mr. Konstantinos Loukelis using MC3T3-E1 mouse osteoblast cells. As indicated by the biological results presented in Figure 2.20, both hydrogels exhibited excellent biocompatibility when compared to the TCPS control substrate, while the preosteoblasts showed a slightly increased proliferation when incubated with the G20D20HAp50 hydrogel in comparison to the G20D20 sample at later time points. Moreover, as observed in the confocal images, the osteoblasts readily proliferated within the G20D20HAp50 hydrogel even at the early time intervals, while for the G20D20 analogue, a less organized cell growth was observed.

Alkaline phosphatase activity of MC3T3-E1 cells incubated with the G20D20 and G20D20HAp50 hydrogels, indicative of the osteogenic differentiation of the cells, was measured on day 7 and day 14, and the respective results are presented in Figure 2.20. At earlier timepoints (day 7), a lower ALP activity compared to the TCPS was observed for both G20D20 and G20D20HAp50, while after 14 days, the ALP activity exhibited an over two-fold increase for both the hydrogels and the TCPS control. The highest ALP activity was found for G20D20HAp50, which is expected due to the incorporation of the nHAp nanoparticles and signifies the differentiation potential of the preosteoblasts to mature osteoblasts.

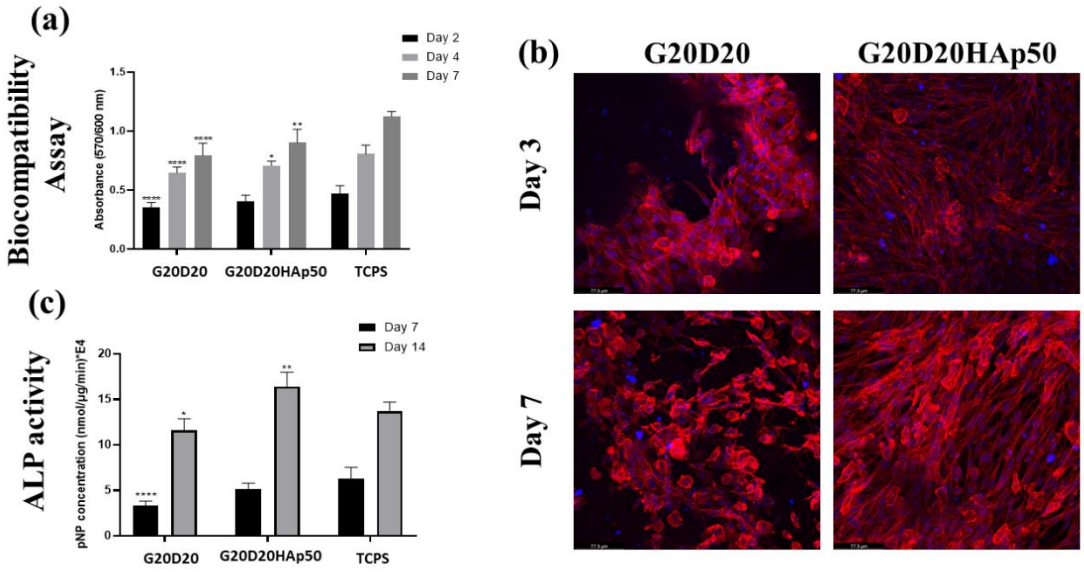

Figure 2.20 - In vitro cellular response on the composite hydrogels. (a) Biocompatibility assay measurements of MC3T3-E1 cells for G20D20, G20D20HAp50 and TCPS (used as a control), on days 2, 4 and 7 of cell culture. (b) Confocal images of the cells on the G20D20 and G20D20HAp50 samples on days 3 and 7 of cell culture. Nuclei are colored in blue with DAPI and the cytoskeleton red with actin. (c) ALP activity measurements of the MC3T3-E1 cells for G20D20, G20D20H50 and the TCPS control on days 7 and 14 of cell culture using osteogenic medium.

2.3.5 Optical and adhesive properties of the GelMA-*co*-DMA hydrogels

The synthesized GelMA-*co*-DMA hydrogels exhibited several other intriguing properties, such as optical transparency, fluorescence under UV light and strong adhesion onto surfaces, as observed in Figure 2.21.

The optical transparency of the hydrogels (Fig. 2.21a) indicated a high degree of dispersion of the thermally exfoliated g-C_3N_4, which was attributed to its steric stabilization by the polymer chains, as proposed in previous studies[87,90,107]. Therefore, artifacts leading to reduced cell viability, such as the precipitation of the initiator on the seeded cells, is eliminated in the case of the polymer hydrogels. In addition, the synthesized hydrogels presented intense fluorescence (Fig. 2.21b), due to the inherent fluorescent properties of the tri-s-triazine units present in the structure of g-C_3N_4[104]. Even when relatively low concentrations of g-C_3N_4 (0.03 wt%) were used, the fluorescent properties of the hydrogels were still quite intense. Furthermore, owing to the incorporation of dopamine methacrylamide as a catechol containing comonomer,

the hydrogels demonstrated strong adhesion onto surfaces, as it can be seen in Fig. 2.21c.

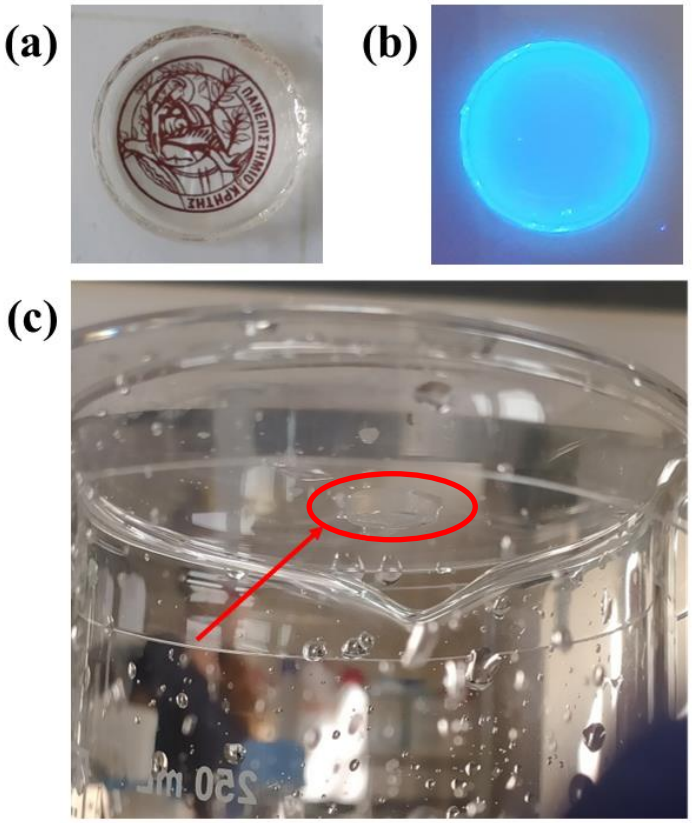

Figure 2.21 - (a) An optically clear GelMA-*co*-DMA hydrogel (G20D20) swollen in DMSO; (b) Fluorescence of a GelMA-*co*-DMA hydrogel (G20D20) under UV light (λ = 365 nm); (c) adhesion of a GelMA-*co*-DMA hydrogel (G20D40) turned upside-down onto a plastic surface.

The combination of these properties, highlight the suitability of the synthesized hydrogels for other potential biological applications, in the field of fluorescent bioimaging and biosensing[127], in biological applications requiring strong material adhesion, such as wound healing[128] or ocular applications[129], and in the field of theranostics[130,131].

2.3.6 Photoinitiated hydrogel synthesis using gCNQDs

A G20D20QDs hydrogel synthesis was performed using gCNQDs at a concentration of 0.03 wt% as a highly efficient, water dispersible, photoinitiator to replace g-C_3N_4,

under similar reaction conditions to those reported above for the G20D20 hydrogel syntheses.

The G20D20QDs hydrogel exhibited an ON/OFF fluorescence when exposed to longwave UV light (λ = 365 nm) due to the inherent fluorescent ability of the gCNQDs[101], similar to the optical properties discussed above for the g-C_3N_4 photoinitiated hydrogel analogue.

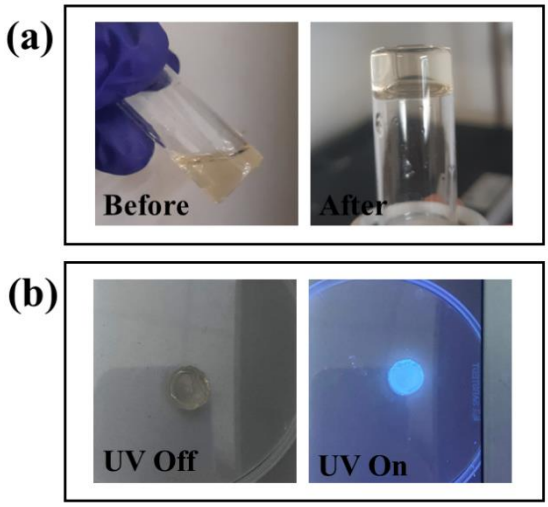

Figure 2.22 - Photographs (a) of G20D20QDs before and after photopolymerization, and (b) of the ON/OFF fluorescence of the G20D20QDs hydrogel right after polymerization

The synthesized hydrogel was also characterized in terms of its degree of swelling and degradation profile. A slight increase in the maximum degree of swelling for the G20D20QDs hydrogel was found in comparison to the G20D20 hydrogel (Figure 2.23). This was attributed to the reduced polymer chain mobility due to the steric hindrance imposed by the incorporation of the g-C_3N_4 nanosheets and crystallites, of a significant lateral size, in the G20D20 sample. Due to the smaller size of the gCNQDs[101], this effect would not be observed for the G20D20QDs hydrogel. On the other hand, the hydrogel stability was not compromised by the incorporation of the gCNQDs as the initiator, instead of the thermally exfoliated g-C_3N_4, and both G20D20 and G20D20QDs samples retained their mass up to 21 d in PBS at 37 ^{o}C.

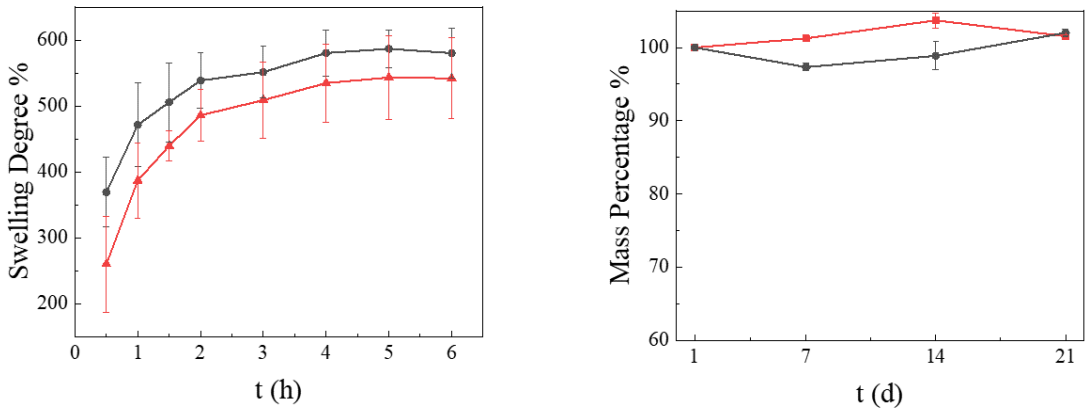

Figure 2.23 - Degrees of swelling (left) and degradation profiles (right) over time for the G20D20QDs (black) and G20D20 (red) hydrogels.

The morphological characterization of the G20D20QDs hydrogel (Figure 2.23) revealed a highly interconnected porous mesh and well-defined pores with relatively thick walls, while an irregular size distribution, with a maximum at ~5.5 μm, was obtained after SEM image analysis using the ImageJ image processing software.

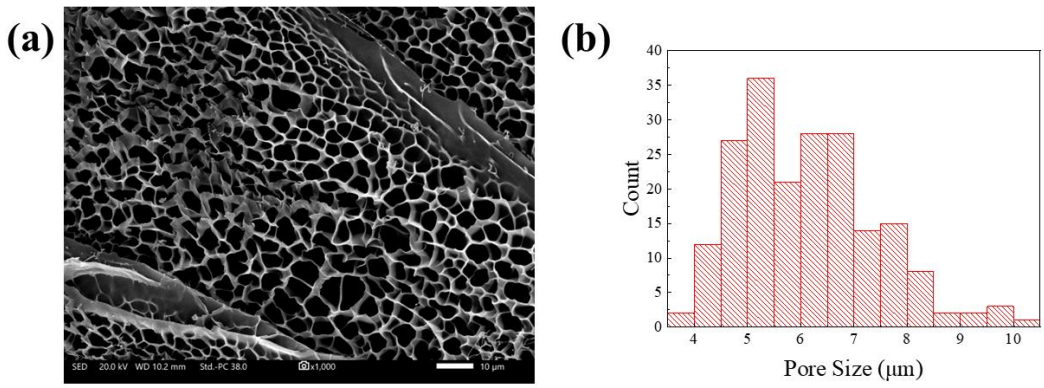

Figure 2.24 - (a) SEM images and (b) pore size distribution of the freeze-dried G20D20QDs hydrogel.

2.4 Conclusions

In conclusion, g-C_3N_4 was synthesized by thermal polycondensation of melamine, and two exfoliation methods were investigated for the preparation of g-C_3N_4 nanosheets, namely thermal exfoliation and liquid exfoliation in water. The successful synthesis of bulk and thermally exfoliated g-C_3N_4 were confirmed by ATR-FTIR spectroscopy and their lattice structure was characterized by XRD. Diffuse reflectance spectroscopy

measurements revealed a similar bandgap of 2.72 eV for both samples. The morphology of the synthesized bulk material and nanosheets was observed via FESEM and the cytocompatibility of the two exfoliated materials was investigated, revealing a 60% - 70% viability for both samples. Next, thermally exfoliated g-C_3N_4 was employed as a visible light photoinitiator for the photo-initiated free radical polymerization of in-house synthesized methacrylamide derivatives of gelatin and dopamine, GelMA and DMA, to form GelMA-*co*-DMA hydrogels. The swelling behavior and the stability of the hydrogels over time in simulated physiological conditions, as well as their morphology, were affected by the degree of functionalization of GelMA and the GelMA and DMA concentration in the precursor solution, and by the irradiation time. Increasing the concentration of both GelMA and DMA, higher degrees of functionalization of the GelMA prepolymer and longer exposure times led to a decrease in the degree of swelling of the hydrogel, but at the same time to superior stability (up to 21 d in PBS) due to the formation of denser porous meshes. Finally, the photoinitiating ability of gCNQDs was also investigated and a G20D20QDs hydrogel was successfully synthesized. All hydrogels synthesized, using either the thermally exfoliated g-C_3N_4 nanosheets or the gCNQDs as the photoinitiator, were optically clear, exhibited intense fluorescence under UV light and strong adhesion properties onto glass and plastic surfaces.

Composite hydrogels, incorporating GelMA, DMA and commercially available nHAp particles, were also synthesized. ATR-FTIR spectroscopy and XRD measurements were used to confirm the successful incorporation of the nanoparticles within the hydrogels, while TGA analysis of the materials verified the quantitative incorporation of the inorganic nanoparticles. The degrees of swelling and the stability over time of the composite hydrogels were found to be affected by the concentration of the nHAp. Increasing nHAp concentration, resulted in hydrogels with lower degrees of swelling, while the synthesized hydrogels maintained their stability in simulated physiological conditions for 21 d. The morphology of the composite hydrogels was also slightly affected by the incorporation of nHAp, and the introduced structural heterogeneity resulted in the formation of slightly larger pores compared to the bare hydrogels. G20D20 and G20D20HAp50 hydrogels were investigated as scaffolds for bone-tissue

regeneration applications. Cell proliferation and viability experiments showed a slightly higher proliferation rate and superior ALP activity of the MC3T3-E1 preosteoblasts on the composite scaffold, also evident from the confocal microscopy images. In future work, the mechanical properties and the hydrophilicity of the composite scaffolds will be investigated, while preliminary results of the photoinitiated polymerization under ambient conditions to prepare GelMA-*co*-DMA hydrogels as cell bioinks are presented in the following chapter.

Chapter 3: Synthesis of GelMA-*co*-DMA hydrogel bioinks

3.1 Introduction

Scaffold morphology is an important factor in the regulation of cell fate for tissue engineering applications. The macroporous properties of the scaffolds have been shown to have a significant impact in guiding tissue growth and differentiation[121]. Even though conventional approaches such as freeze-drying and gas foaming have been used to obtain and control the size and porosity of hydrogel scaffolds[33], these techniques are limited when the fabrication of complex geometries is required. Additive manufacturing technologies such as 3D bioprinting can provide the means to overcome these limitations. Cell laden bioinks can be used to fabricate complex 3D structures and can provide a template for homogeneous cell seeding[7,33]. The use of photopolymerizable bioinks, offers many advantages (mild reaction conditions, fast cross-linking, room temperature operation) in this direction, but is hindered by the cell toxicity induced by the use of UV light and the oxygen inhibition of the free radical polymerization.[72,132] To overcome this limitation, the use of g-C_3N_4 nanosheets in the presence of triethanolamine (TEOA) as a cocatalyst, was explored herein towards the oxygen tolerant preparation of both GelMA-*co*-DMA and GelMA water-swollen hydrogels and some preliminary results are presented below.

3.2. Materials and Methods

3.2.1 Materials

Dopamine hydrochloride (99%) and melamine (99%) were purchased from Alfa Aesar. Methacrylic anhydride (94%), N,N'-methylenebisacrylamide (MBA, 97%) and sodium tetraborate (>99.5%), were provided by Aldrich. PBS tablets and Gelatin Type B from Bovine Skin (225g Bloom) were supplied by Sigma, while sodium hydroxide pellets were obtained from Panreac. Sodium bicarbonate (99.7%) and triethanolamine (99%) were purchased from Sigma Aldrich and hydrochloric acid was purchased from

Scharlau. All solvents were supplied by Sigma Aldrich and were used as received. Milli-Q water was used for the preparation of all samples and was obtained from a Millipore apparatus with a resistivity of 18.2 MΩ at 298 K.

3.2.2 Methods

3.2.2.1 Synthesis of gelatin methacrylate and dopamine methacrylamide

Methacrylamide derivatives of gelatin and dopamine were prepared as described in the experimental section of Chapter 2.

3.2.2.2 g-C_3N_4/Triethanolamine as an oxygen tolerant photoinitiator system to obtain GelMA and GelMA-*co*-DMA hydrogels

GelMA hydrogels were prepared using g-C_3N_4/Triethanolamine (TEOA) as a photoinitiator system (PIS) following a modified method proposed by F. Parra et al.[133] to investigate the ability of the system to initiate the photopolymerization at ambient conditions. The reaction conditions employed are presented in Table 3.1. In the following, the hydrogels synthesized in the presence of DMA will be denoted as GxDyTEOA, where x refers to the wt% of GelMA in the precursor solution and y to the DMA mol% ratio over the GelMA monomer repeat units, while the plain GelMA hydrogels, synthesized using only GelMA with different degrees of functionalization will be denoted as GzFwTEOA, where z refers to the wt% of GelMA in the precursor solution and w to its degree of functionalization.

The synthesis of G20D20TEOA is described below as a model synthesis. Briefly, in a 4 ml vial, 100 mg GelMA II (degree of functionalization 43%) were dissolved in 100 mg milliQ water and 200 mg ethylene glycol, under stirring at 37 ^{o}C overnight. Then, 8 mg DMA were added in the solution. Finally, 100 mg of a g-C_3N_4/TEOA aqueous dispersion, prepared at a 1.5 mg/g concentration of thermally exfoliated g-C_3N_4 and an 8.1 mg/g concentration of TEOA in water, were added in the first solution to generate

a final dispersion with a 0.03 wt% g-C_3N_4 and a 40:1 molar ratio of GelMA monomer repeat units over TEOA.

Table 3.1 - Reaction conditions for the synthesis of the GelMA and GelMA-*co*-DMA hydrogels using g-C_3N_4/TEOA as the photoinitiator system

Sample*	GelMA wt%	DMA/monomer repeat units of GelMA mol %	Solvent milliQ:ethylene glycol	GelMA DoF
G20D20TEOA	20	20	1:1	43%
G20D40TEOA	20	40	1:1	43%
G20F40TEOA	20	0	1:0	43%
G20F60TEOA	20	0	1:0	56%

*g-C_3N_4 **:**0.03wt%, GelMA:TEOA 40:1 moles

Next, the precursor solution was transferred to a 96 well plate and was photopolymerized using a long wave UV lamp at λ = 365 nm, while the temperature of the plate was kept constant at 37 ^oC. After gelation, the gels were retrieved from the wells, and following extensive washing with water to remove any unreacted materials, they were finally transferred to PBS at 37 ^oC to study their degradation profile.

3.2.2.3 GelMA hydrogels using *N,N'*-Methylenebisacrylamide as the cross-linker and g-C_3N_4/TEOA as the photoinitiator system.

The preparation of GelMA hydrogels using *N,N'*-Methylenebisacrylamide (MBA) as the cross-linker and g-C_3N_4/TEOA as the PIS was studied. For this, the effect of GelMA concentration on the photopolymerization and gelation of aqueous droplets in the presence of oxygen was evaluated. Briefly, three different concentrations of GelMA in the precursor solution were investigated, namely 20%, 30% and 40%, while the photoinitiator concentration and the cross-linker molar ratio over the monomer repeat units of GelMA, were kept constant at 0.03 wt% and 10 mol%, respectively as shown

in Table 3.2. In the following the synthesized hydrogel droplets will be denoted as GxMy, where x refers to the wt% of GelMA in the precursor solution and y to the MBA mol% ratio over the GelMA monomer repeat units.

Table 3.2 - Reaction conditions for the GelMA hydrogel droplets using g-C_3N_4/TEOA as the photoinitiator system

Sample*	GelMA wt%	MBA over GelMA monomer repeat units mol %	GelMA+MBA:TEOA Mole ratio
G20M10	20	10	40:1
G30M10	30	10	40:1
G40M10	40	10	40:1

*g-C_3N_4: 0.03 wt%

Droplets of each of the precursor solutions were deposited onto glass substrates thermostated at 37 ^oC using a hot plate and were photopolymerized for 5, 10 and 20 min by a longwave UV lamp (λ = 365 nm). The gelled droplets were then kept in aqueous environment at RT for one week and were subsequently transferred in PBS at 37 ^oC to characterize their stability.

3.3 Results and Discussion

3.3.1 GelMA-*co*-DMA hydrogels synthesized at ambient conditions

GelMA-*co*-DMA hydrogels were synthesized by photopolymerization using g-C_3N_4/TEOA as the photoinitiator system under UV light irradiation (λ = 365 nm) at 37 ^oC and ambient conditions. The proposed reaction mechanism for the presented PIS is illustrated in Figure 5.1. Upon light irradiation of the precursor solution containing g-C_3N_4, simultaneous excitation of electrons from the valence band to the conduction band (E_g = 2.72 eV) and creation of holes in the valence band of g-C_3N_4 takes place.[134]

At ambient conditions, negatively charged electrons in the conduction band enable oxygen reduction via electron transfer from O_2 to $O_2^{\cdot -}$ [135]. After disproportionation, these superoxides can form H_2O_2, which reacts with the tertiary amine (TEOA) to form H_2O, thus resulting in oxygen removal[136,137]. The formation of initiating radicals is promoted by the generation of positively charged holes in the valence band. These holes can oxidize electron donors such as TEOA, which in turn produce TEOA cations by hydrogen abstraction from another TEOA molecule, that can initiate the polymerization reaction[88,89].

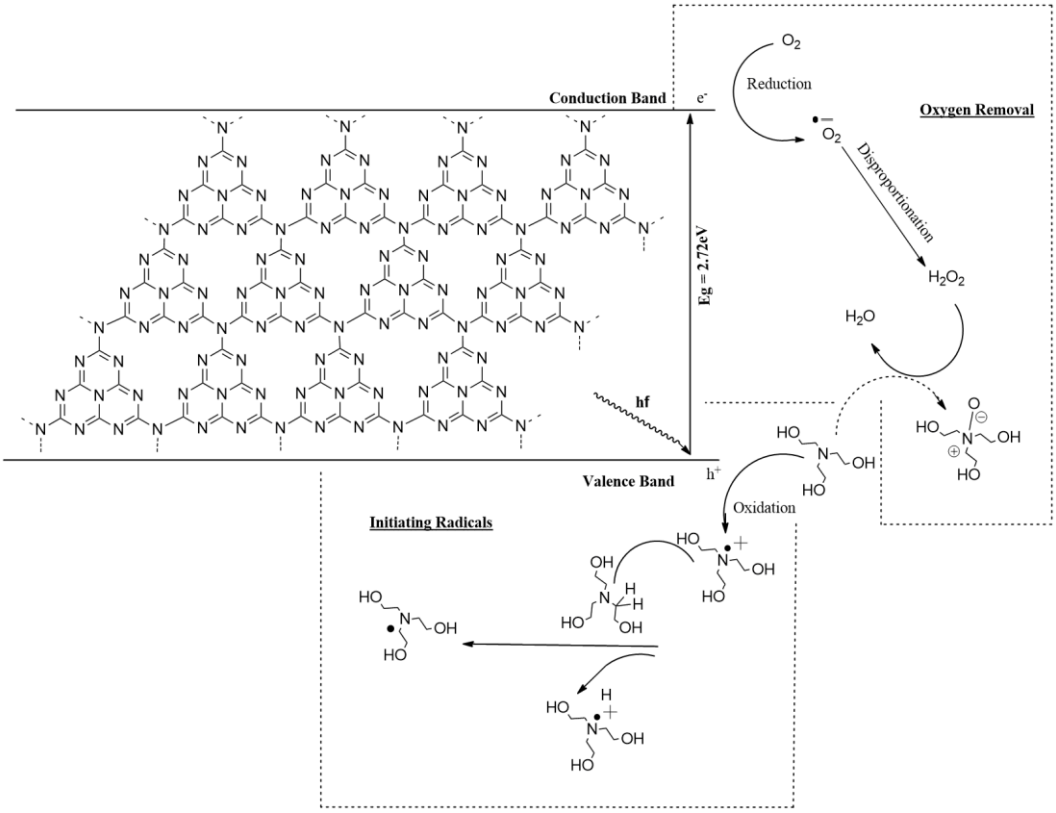

Figure 3.1 - Proposed reaction mechanism for the g-C_3N_4/TEOA PIS at ambient conditions

Here the ability of the g-C_3N_4/TEOA PIS to induce photopolymerization in the presence of oxygen was studied, along with the effects of the degree of functionalization of GelMA and the molar ratio of DMA over the monomer repeat units of GelMA. Gelation for the GxDyTEOA solution was observed after 2 h of irradiation (Figure 3.2). The hydrogels appeared to have a brownish hue, probably due to catechol oxidation from TEOA[138,139] which can induce catechol tanning[140]. Also in this system, ethylene glycol

is employed as a cosolvent, since DMA is highly hydrophobic and cannot be dissolved in water[140,141]. The introduction of ethylene glycol can slightly increase the viscosity of the precursor solution and in turn influence oxygen diffusion[142,143] and depletion[132] and thus result in a more efficient polymerization. GxFyTEOA hydrogels were irradiated for 4 h and an incomplete gelation was observed throughout the volume of the precursor solution.

Figure 3.2 - Photographs of G20D40TEOA (left) and G20D20TEOA (middle) after 2 h photopolymerization. Photographs of all gels after their transfer into PBS. The hydrogels are shown by arrows of different colors for G20D20TEOA (black), G20D40TEOA (red), G20F40TEOA (blue), G20F60TEOA (green).

3.3.1.1 Stability of the GelMA-*co*-DMA hydrogels synthesized at ambient conditions

The stability of the GelMA-*co*-DMA hydrogels obtained at ambient conditions was followed and quantified over 10 d under simulated physiological conditions (PBS, 37 ^{o}C). The in vitro degradation profiles of the hydrogels are presented in Figure 3.2. Higher concentrations of DMA in the precursor solution resulted in an enhanced stability of the hydrogels, while in the absence of DMA rapid degradation occurred and a mass loss of approximately 50% was observed for G20F40TEOA in the first 3 d compared to 23% and 13%, for G20D20TEOA and G20D40TEOA, respectively. After 10 d the remaining mass for G20D40TEOA and G20D20TEOA were found approximately equal to 73% and 57%, while for the plain G20F40TEOA hydrogel the remaining mass was calculated at 14%. It is thus concluded that in the absence of DMA, a higher degree of functionalization of GelMA ensured the higher stability of the hydrogel, but still inferior to the stability of the GelMA-*co*-DMA hydrogels. A minimal mass loss was observed for the G20F60TEOA hydrogel in the first 3 d approximately

equal to 10% and a rapid decline on the 4th day leading to a mass loss of approximately 50% and a total remaining mass of 40% after 10 days, significantly higher compared to that of G20F40. This phenomenon, as previously discussed, is associated to the cross-link density of the hydrogels. Higher degrees of modification of the photopolymer can be beneficial for the synthesis of hydrogels of higher cross-link densities[10,55] and thus provide superior stability. This also applies for the DMA containing hydrogels, since via catechol self-cross-linking[58], a secondary cross-linking mechanism is also provided and thus a higher cross-link density can be achieved. In either case, increasing the presence of methacrylamide groups in the precursor solution had a positive effect and drive forward the polymerization[143].

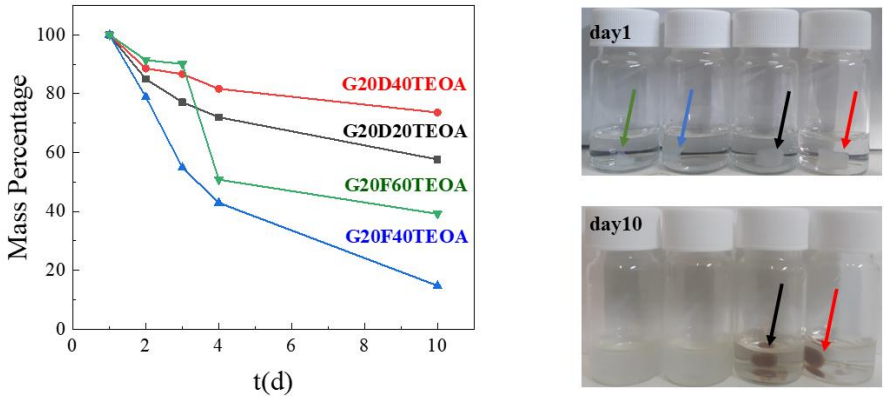

Figure 3.2 - Degradation profiles of the GelMA-*co*-DMA hydrogels synthesized at ambient conditions (left) and photographs of the hydrogels in PBS on day 1 (top right) and day 10 (down right). G20D20TEOA (black ■), G20D40TEOA (red ●), G20F40TEOA (blue ▲), G20F60TEOA (green ▼) hydrogels.

3.3.2 Photopolymerization of aqueous GelMA droplets.

Since ethylene glycol has been shown to exhibit cell toxicity[144–146], we also investigated the synthesis of GelMA bioinks using the water-soluble cross-linker MBA, eliminating thus the need for the presence of ethylene glycol in the precursor solution. Accordingly, TEOA levels used were significantly lower than the proposed levels in the literature[147] and the US7427415B2 patent on the "Implantation of encapsulated biological materials for treating diseases[148], with the highest concentration of TEOA in the aqueous droplets being approximately equal to 3.3 mM and the proposed range of TEOA in the patent being 5 mM to 2 M. The photopolymerization of aqueous droplets of GelMA, using

MBA and g-C_3N_4/TEOA as the PIS under UV light irradiation (λ = 365 nm) at 37 °C, is thus expected to simulate more efficiently the conditions used for bioprinting of 3D scaffolds.

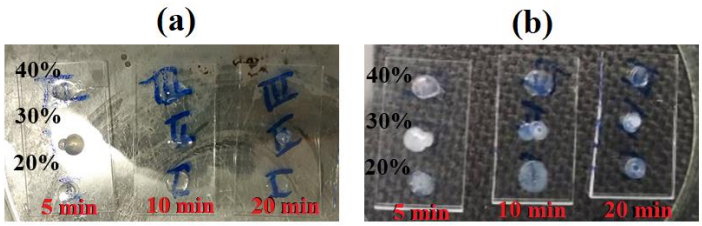

Figure 3.3 - Photographs of aqueous droplets of GelMA at 20 wt%, 30 wt% and 40 wt% concentration in water before (a) and after (b) exposure to UV light for 5 min, 10 min and 20 min.

Cross-linking was achieved for all droplets even for short exposure times, such as 5 min, as shown in Fig. 3.3. The cross-linked droplets were next transferred to a 12-well plate and their stability against PBS was studied via optical observation of their inherent fluorescence under UV light[92,93]. In Figure 3.4, the cross-linked droplets are shown, over 14 d in PBS at 37 °C, under UV light.

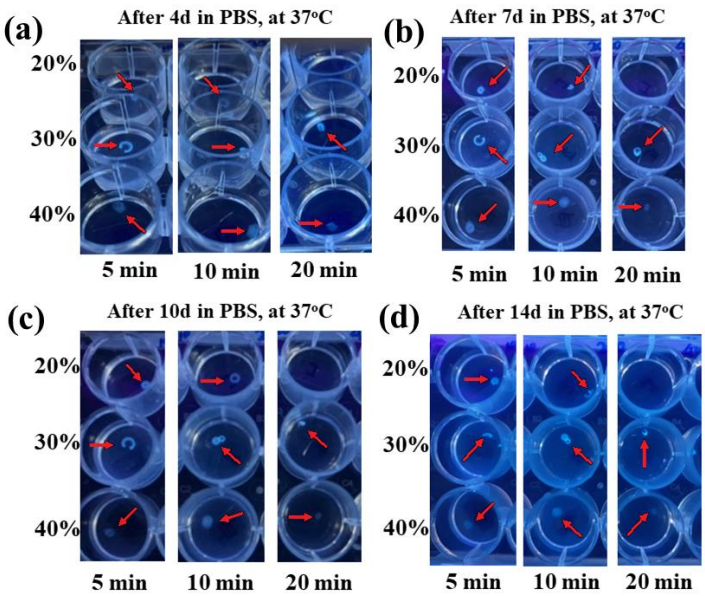

Figure 3.4 - Photographs of water-based cross-linked droplets, at different days in PBS at 37 °C (a-d). Droplets are illuminated with UV light (λ = 365 nm) and the fluorescence of g-C_3N_4 is used to detect them in the surrounding solvent.

The cross-linked GelMA droplets appeared to be stable at least for 7 days in PBS. However, a slight degradation was observed after 7 days, as evidenced by the increase of the turbidity of the surrounding medium from clear to slightly milky. Nevertheless, the GelMA cross-linked droplets were still present in most of the wells after 14 days in PBS, signifying their promising stability for future application as bioinks.

3.4 Conclusions and Future Work

In conclusion, the successful photoinitiated free-radical polymerization of GelMA and GelMA-DMA mixtures to give GelMA and GelMA-*co*-DMA hydrogels under aerobic conditions, using g-C_3N_4/TEOA as the photoinitiator system, was demonstrated. The stability of the hydrogels, synthesized in the absence of a crosslinker, under simulated physiological conditions (pH 7.4 and 37 ^oC) was affected by the degree of functionalization of GelMA and the concentration of DMA over the monomer repeat units of GelMA. Higher degrees of functionalization of GelMA and the increase of the DMA concentration contributed to the prolonged stability of the hydrogels. The superior stability of the GelMA-*co*-DMA hydrogels compared to the GelMA hydrogels, suggested the contribution of DMA to a higher cross-link density and signified the potential of the GelMA-*co*-DMA hydrogels in 3D bioprinting to obtain constructs with tailored morphology. To better simulate the bioprinting conditions in the presence of cells, aqueous droplets of GelMA (in the absence of ethylene glycol) were photopolymerized under aerobic conditions, at 37 ^oC using g-C_3N_4/TEOA as the PIS and MBA as a water-soluble cross-linker. Concentrations of TEOA, significantly lower than those reported in the literature, enabled the fast gelation of the droplets under aerobic conditions after on 5 min irradiation time. The synthesized gels were found to be stable under simulated physiological conditions up to at least 14 days in PBS at 37 ^oC suggesting the potential application of such formulations as cell-laden bioinks. In future work, rheological experiments should be conducted to ensure the printability of the aqueous GelMA formulations, followed by the 3D printing of the hydrogels and the evaluation of the structural fidelity of the 3D constructs (stability and mechanical properties). Finally, 3D bioprinting of cell-laden bioinks and their biological evaluation will be conducted (cell viability, biodegradation, cell proliferation and differentiation).

References

1. Choi, J. R., Yong, K. W., Choi, J. Y. & Cowie, A. C. Recent advances in photo-crosslinkable hydrogels for biomedical applications. *BioTechniques* **66**, 40–53 (2019).
2. Hoffman, A. S. Hydrogels for biomedical applications. *Advanced Drug Delivery Reviews* **64**, 18–23 (2012).
3. Musgrave, C. S. A. & Fang, F. Contact Lens Materials: A Materials Science Perspective. *Materials* **12**, 261 (2019).
4. Hydrogel-based composites: Unlimited platforms for biosensors and diagnostics - Wang - 2021 - VIEW - Wiley Online Library. https://onlinelibrary.wiley.com/doi/full/10.1002/VIW.20200165.
5. Dreiss, C. A. Hydrogel design strategies for drug delivery. *Current Opinion in Colloid & Interface Science* **48**, 1–17 (2020).
6. Gomez-Florit, M. *et al.* Natural-Based Hydrogels for Tissue Engineering Applications. *Molecules* **25**, 5858 (2020).
7. Nguyen, K. T. & West, J. L. Photopolymerizable hydrogels for tissue engineering applications. *Biomaterials* **23**, 4307–4314 (2002).
8. Ji, Q. *et al.* Hydrosoluble collagen based biodegradable hybrid hydrogel for biomedical scaffold. *Journal of Biomaterials Science, Polymer Edition* **31**, 2199–2219 (2020).
9. Sun, H. *et al.* Carbon nanotube-incorporated collagen hydrogels improve cell alignment and the performance of cardiac constructs. *IJN* **Volume 12**, 3109–3120 (2017).
10. Nichol, J. W. *et al.* Cell-laden microengineered gelatin methacrylate hydrogels. *Biomaterials* **31**, 5536–5544 (2010).
11. Fonseca, D. F. S. *et al.* Swellable Gelatin Methacryloyl Microneedles for Extraction of Interstitial Skin Fluid toward Minimally Invasive Monitoring of Urea. *Macromol. Biosci.* **20**, 2000195 (2020).
12. Osi, A. R. *et al.* Three-Dimensional-Printable Thermo/Photo-Cross-Linked Methacrylated Chitosan–Gelatin Hydrogel Composites for Tissue Engineering. *ACS Appl. Mater. Interfaces* **13**, 22902–22913 (2021).
13. Ma, P. *et al.* Biomimetic gelatin/chitosan/polyvinyl alcohol/nano-hydroxyapatite scaffolds for bone tissue engineering. *Materials & Design* **207**, 109865 (2021).
14. Velasco-Rodriguez, B. *et al.* Hybrid Methacrylated Gelatin and Hyaluronic Acid Hydrogel Scaffolds. Preparation and Systematic Characterization for Prospective Tissue Engineering Applications. *International Journal of Molecular Sciences* **22**, 6758 (2021).
15. Li, H. *et al.* The Application of Hyaluronic Acid-Based Hydrogels in Bone and Cartilage Tissue Engineering. *Advances in Materials Science and Engineering* **2019**, e3027303 (2019).
16. Aldana, A. A., Valente, F., Dilley, R. & Doyle, B. Development of 3D bioprinted GelMA-alginate hydrogels with tunable mechanical properties. *Bioprinting* **21**, e00105 (2021).
17. Araiza-Verduzco, F. *et al.* Photocrosslinked Alginate-Methacrylate Hydrogels with Modulable Mechanical Properties: Effect of the Molecular Conformation and Electron Density of the Methacrylate Reactive Group. *Materials* **13**, 534 (2020).
18. Charron, P. N., Garcia, L. M., Tahir, I. & Floreani, R. Bio-inspired green light crosslinked alginate-heparin hydrogels support HUVEC tube formation. *Journal of the Mechanical Behavior of Biomedical Materials* **125**, 104932 (2022).
19. Heparin-based and heparin-inspired hydrogels: size-effect, gelation and biomedical applications - Journal of Materials Chemistry B (RSC Publishing). https://pubs.rsc.org/en/content/articlelanding/2019/tb/c8tb02671h/unauth.
20. Aguilar-de-Leyva, Á., Linares, V., Casas, M. & Caraballo, I. 3D Printed Drug Delivery Systems Based on Natural Products. *Pharmaceutics* **12**, 620 (2020).

21. Zhang, F. & King, M. W. Biodegradable Polymers as the Pivotal Player in the Design of Tissue Engineering Scaffolds. *Adv. Healthcare Mater.* **9**, 1901358 (2020).
22. Liu, Y. *et al.* Injectable Dopamine-Modified Poly(ethylene glycol) Nanocomposite Hydrogel with Enhanced Adhesive Property and Bioactivity. *ACS Appl Mater Interfaces* **6**, 16982–16992 (2014).
23. Gaharwar, A. K., Dammu, S. A., Canter, J. M., Wu, C.-J. & Schmidt, G. Highly Extensible, Tough, and Elastomeric Nanocomposite Hydrogels from Poly(ethylene glycol) and Hydroxyapatite Nanoparticles. *Biomacromolecules* **12**, 1641–1650 (2011).
24. He, Y. *et al.* A photocurable hybrid chitosan/acrylamide bioink for DLP based 3D bioprinting. *Materials & Design* **202**, 109588 (2021).
25. Han, L. *et al.* Biohybrid methacrylated gelatin/polyacrylamide hydrogels for cartilage repair. *J. Mater. Chem. B* **5**, 731–741 (2017).
26. Chakka, J., Laird, N., Acri, T., Elangovan, S. & Salem, A. Polydopamine Functionalized 3D Printed Scaffolds for Bone Tissue Engineering. *Transactions on Additive Manufacturing Meets Medicine* Vol 2 No 1 (2020): Trans. AMMM (2020) doi:10.18416/AMMM.2020.2009020.
27. Perinelli, D. R., Cespi, M., Bonacucina, G. & Palmieri, G. F. PEGylated polylactide (PLA) and poly (lactic-co-glycolic acid) (PLGA) copolymers for the design of drug delivery systems. *J. Pharm. Investig.* **49**, 443–458 (2019).
28. Hosseini, V., Evrova, O., Hoerstrup, S. P. & Vogel, V. A Simple Modification Method to Obtain Anisotropic and Porous 3D Microfibrillar Scaffolds for Surgical and Biomedical Applications. *Small* **14**, 1702650 (2018).
29. Formation of Neoarteries with Optimal Remodeling Using Rapidly Degrading Textile Vascular Grafts | Tissue Engineering Part A. https://www.liebertpub.com/doi/10.1089/ten.tea.2018.0167.
30. Li, H., Zheng, L. & Wang, M. Biofunctionalized Nanofibrous Bilayer Scaffolds for Enhancing Cell Adhesion, Proliferation and Osteogenesis. *ACS Appl. Bio Mater.* **4**, 5276–5294 (2021).
31. Physically crosslinked polyvinyl alcohol hydrogels as synthetic cartilage materials: Annals of Medicine: Vol 53, No sup1. https://www.tandfonline.com/doi/abs/10.1080/07853890.2021.1896904.
32. Poorna, M. R., Jayakumar, R., Chen, J.-P. & Mony, U. Hydrogels: A potential platform for induced pluripotent stem cell culture and differentiation. *Colloids and Surfaces B: Biointerfaces* **207**, 111991 (2021).
33. Elkhoury, K. *et al.* Biofabrication of natural hydrogels for cardiac, neural, and bone Tissue engineering Applications. *Bioactive Materials* **6**, 3904–3923 (2021).
34. Bahram, M., Mohseni, N. & Moghtader, M. An Introduction to Hydrogels and Some Recent Applications. in *Emerging Concepts in Analysis and Applications of Hydrogels* (ed. Majee, S. B.) (InTech, 2016). doi:10.5772/64301.
35. Yahia, Lh. History and Applications of Hydrogels. *J Biomed Sci* **04**, (2015).
36. Williams, D. F. On the mechanisms of biocompatibility. *Biomaterials* **29**, 2941–2953 (2008).
37. Jurak, M., Wiącek, A. E., Ładniak, A., Przykaza, K. & Szafran, K. What affects the biocompatibility of polymers? *Advances in Colloid and Interface Science* **294**, 102451 (2021).
38. WICHTERLE, O. & LÍM, D. Hydrophilic Gels for Biological Use. *Nature* **185**, 117–118 (1960).
39. Mozafari, M., Sefat, F. & Atala, A. Handbook of Tissue Engineering Scaffolds: Volume One. 759.
40. O'Brien, F. J. Biomaterials & scaffolds for tissue engineering. *Materials Today* **14**, 88–95 (2011).

41. Bauer, S., Schmuki, P., von der Mark, K. & Park, J. Engineering biocompatible implant surfaces. *Progress in Materials Science* **58**, 261–326 (2013).
42. *Biomedical Applications of Hydrogels Handbook*. (Springer New York, 2010). doi:10.1007/978-1-4419-5919-5.
43. Chan, B. P. & Leong, K. W. Scaffolding in tissue engineering: general approaches and tissue-specific considerations. *Eur Spine J* **17**, 467–479 (2008).
44. Van Der Rest, M. & Garrone, R. Collagen family of proteins. *FASEB j.* **5**, 2814–2823 (1991).
45. Ruoslahti, E. RGD AND OTHER RECOGNITION SEQUENCES FOR INTEGRINS. *Annu. Rev. Cell Dev. Biol.* **12**, 697–715 (1996).
46. Ananta, M. *et al.* A Poly(Lactic Acid-Co-Caprolactone)–Collagen Hybrid for Tissue Engineering Applications. *Tissue Engineering Part A* **15**, 1667–1675 (2009).
47. Tatiana, N. M., Cornelia, V., Tatia, R. & Aurica, C. Hybrid collagen/pNIPAAM hydrogel nanocomposites for tissue engineering application. *Colloid Polym Sci* **296**, 1555–1571 (2018).
48. Heinemann, S. *et al.* Effect of Silica and Hydroxyapatite Mineralization on the Mechanical Properties and the Biocompatibility of Nanocomposite Collagen Scaffolds. *ACS Appl. Mater. Interfaces* **3**, 4323–4331 (2011).
49. Lukin, I. *et al.* Progress in Gelatin as Biomaterial for Tissue Engineering. *Pharmaceutics* **14**, 1177 (2022).
50. Naomi, R., Bahari, H., Ridzuan, P. M. & Othman, F. Natural-Based Biomaterial for Skin Wound Healing (Gelatin vs. Collagen): Expert Review. *Polymers (Basel)* **13**, 2319 (2021).
51. Nishinari, K. *et al.* The Effect of Sucrose on the Thermo-Reversible Gel-Sol Transition in Agarose and Gelatin. *Polym J* **24**, 871–877 (1992).
52. Ramalingam, M. & Ramakrishna, S. *Nanofiber Composites for Biomedical Applications*. (Woodhead Publishing, 2017).
53. Van Den Bulcke, A. I. *et al.* Structural and Rheological Properties of Methacrylamide Modified Gelatin Hydrogels. *Biomacromolecules* **1**, 31–38 (2000).
54. Göckler, T. *et al.* Tuning Superfast Curing Thiol-Norbornene-Functionalized Gelatin Hydrogels for 3D Bioprinting. *Advanced Healthcare Materials* **10**, 2100206 (2021).
55. Bencherif, S. A. *et al.* Influence of the degree of methacrylation on hyaluronic acid hydrogels properties. *Biomaterials* **29**, 1739–1749 (2008).
56. Hou, Y., Deng, X. & Xie, C. Biomaterial surface modification for underwater adhesion. *Smart Materials in Medicine* **1**, 77–91 (2020).
57. Chen, S. *et al.* Adhesive Tissue Engineered Scaffolds: Mechanisms and Applications. *Front Bioeng Biotechnol* **9**, 683079 (2021).
58. Quan *et al.* Mussel-Inspired Catechol-Functionalized Hydrogels and Their Medical Applications. *Molecules* **24**, 2586 (2019).
59. Gan, D. *et al.* Mussel-Inspired Tough Hydrogel with In Situ Nanohydroxyapatite Mineralization for Osteochondral Defect Repair. *Adv. Healthcare Mater.* **8**, 1901103 (2019).
60. Costa, P. M. *et al.* Mussel-Inspired Catechol Functionalisation as a Strategy to Enhance Biomaterial Adhesion: A Systematic Review. *Polymers* **13**, 3317 (2021).
61. Kaushik, N. K. *et al.* Biomedical and Clinical Importance of Mussel-Inspired Polymers and Materials. *Marine Drugs* **13**, 6792–6817 (2015).
62. Zhang, W. *et al.* Catechol-functionalized hydrogels: biomimetic design, adhesion mechanism, and biomedical applications. *Chem. Soc. Rev.* **49**, 433–464 (2020).
63. Zhao, P. *et al.* Mussel-mimetic hydrogels with defined cross-linkers achieved via controlled catechol dimerization exhibiting tough adhesion for wet biological tissues. *Chem. Commun.* **53**, 12000–12003 (2017).

64. Han, L. *et al.* Mussel-Inspired Tissue-Adhesive Hydrogel Based on the Polydopamine–Chondroitin Sulfate Complex for Growth-Factor-Free Cartilage Regeneration. *ACS Appl. Mater. Interfaces* **10**, 28015–28026 (2018).
65. Wang, X. *et al.* Discriminating the Independent Influence of Cell Adhesion and Spreading Area on Stem Cell Fate Determination Using Micropatterned Surfaces. *Sci Rep* **6**, 28708 (2016).
66. Wang, Y.-K. & Chen, C. S. Cell adhesion and mechanical stimulation in the regulation of mesenchymal stem cell differentiation. *J Cell Mol Med* **17**, 823–832 (2013).
67. Raja, I. S. *et al.* The predominant factor influencing cellular behavior on electrospun nanofibrous scaffolds: Wettability or surface morphology? *Materials & Design* **216**, 110580 (2022).
68. Pu, X. *et al.* Bioinspired Hydrogel Anchoring 3DP GelMA/HAp Scaffolds Accelerates Bone Reconstruction. *ACS Appl. Mater. Interfaces* **14**, 20591–20602 (2022).
69. Ribas-Massonis, A., Cicujano, M., Duran, J., Besalú, E. & Poater, A. Free-Radical Photopolymerization for Curing Products for Refinish Coatings Market. *Polymers* **14**, 2856 (2022).
70. Kaur, M. & Srivastava, A. K. PHOTOPOLYMERIZATION: A REVIEW. *Journal of Macromolecular Science, Part C: Polymer Reviews* **42**, 481–512 (2002).
71. Tehfe, M., Louradour, F., Lalevée, J. & Fouassier, J.-P. Photopolymerization Reactions: On the Way to a Green and Sustainable Chemistry. *Applied Sciences* **3**, 490–514 (2013).
72. Chiulan, I., Heggset, E. B., Voicu, Ş. I. & Chinga-Carrasco, G. Photopolymerization of Bio-Based Polymers in a Biomedical Engineering Perspective. *Biomacromolecules* **22**, 1795–1814 (2021).
73. Tomal, W. & Ortyl, J. Water-Soluble Photoinitiators in Biomedical Applications. *Polymers* **12**, 1073 (2020).
74. Yang, K.-H. *et al.* Effect of Photoinitiator on Precursory Stability and Curing Depth of Thiol-Ene Clickable Gelatin. *Polymers* **13**, 1877 (2021).
75. Choe, E., Huang, R. & Min, D. B. Chemical Reactions and Stability of Riboflavin in Foods. *Journal of Food Science* **70**, R28–R36 (2005).
76. Shields, H. J., Traa, A. & Van Raamsdonk, J. M. Beneficial and Detrimental Effects of Reactive Oxygen Species on Lifespan: A Comprehensive Review of Comparative and Experimental Studies. *Front. Cell Dev. Biol.* **9**, 628157 (2021).
77. Shao, J., Huang, Y. & Fan, Q. Visible light initiating systems for photopolymerization: status, development and challenges. *Polym. Chem.* **5**, 4195–4210 (2014).
78. Eggersdorfer, M. *et al.* One Hundred Years of Vitamins-A Success Story of the Natural Sciences. *Angew. Chem. Int. Ed.* **51**, 12960–12990 (2012).
79. Gessner, T. & Mayer, U. Triarylmethane and Diarylmethane Dyes. in *Ullmann's Encyclopedia of Industrial Chemistry* (ed. Wiley-VCH Verlag GmbH & Co. KGaA) a27_179 (Wiley-VCH Verlag GmbH & Co. KGaA, 2000). doi:10.1002/ 14356007.a27_179.
80. Sheraz, M. A., Kazi, S. H., Ahmed, S., Anwar, Z. & Ahmad, I. Photo, thermal and chemical degradation of riboflavin. *Beilstein J Org Chem* **10**, 1999–2012 (2014).
81. Herculano, L. S. *et al.* Investigation of the Photobleaching Process of Eosin Y in Aqueous Solution by Thermal Lens Spectroscopy. *J. Phys. Chem. B* **117**, 1932–1937 (2013).
82. Yue, K. *et al.* Synthesis, properties, and biomedical applications of gelatin methacryloyl (GelMA) hydrogels. *Biomaterials* **73**, 254–271 (2015).
83. Wang, X. *et al.* A metal-free polymeric photocatalyst for hydrogen production from water under visible light. *Nature Mater* **8**, 76–80 (2009).
84. Xu, J., Zhang, L., Shi, R. & Zhu, Y. Chemical exfoliation of graphitic carbon nitride for efficient heterogeneous photocatalysis. *J. Mater. Chem. A* **1**, 14766 (2013).

85. Li, Y. *et al.* Macroscopic Foam-Like Holey Ultrathin g-C_3N_4 Nanosheets for Drastic Improvement of Visible-Light Photocatalytic Activity. *Adv. Energy Mater.* **6**, 1601273 (2016).
86. Niu, P., Zhang, L., Liu, G. & Cheng, H.-M. Graphene-Like Carbon Nitride Nanosheets for Improved Photocatalytic Activities. *Adv. Funct. Mater.* **22**, 4763–4770 (2012).
87. Cao, Q., Kumru, B., Antonietti, M. & Schmidt, B. V. K. J. Graphitic carbon nitride and polymers: a mutual combination for advanced properties. *Mater. Horiz.* **7**, 762–786 (2020).
88. Cao, Q., Heil, T., Kumru, B., Antonietti, M. & Schmidt, B. V. K. J. Visible-light induced emulsion photopolymerization with carbon nitride as a stabilizer and photoinitiator. *Polym. Chem.* **10**, 5315–5323 (2019).
89. Kiskan, B., Zhang, J., Wang, X., Antonietti, M. & Yagci, Y. Mesoporous Graphitic Carbon Nitride as a Heterogeneous Visible Light Photoinitiator for Radical Polymerization. *ACS Macro Lett.* **1**, 546–549 (2012).
90. Kumru, B., Shalom, M., Antonietti, M. & Schmidt, B. V. K. J. Reinforced Hydrogels via Carbon Nitride Initiated Polymerization. *Macromolecules* **50**, 1862–1869 (2017).
91. Hang, Z., Yu, H., Luo, L. & Huai, X. Nanoporous g-C3N4/MOF: high-performance photoinitiator for UV-curable coating. *J Mater Sci* **54**, 13959–13972 (2019).
92. Zhang, X. *et al.* Enhanced Photoresponsive Ultrathin Graphitic-Phase C_3N_4 Nanosheets for Bioimaging. *J. Am. Chem. Soc.* **135**, 18–21 (2013).
93. Lin, L.-S. *et al.* Graphitic-phase C3N4 nanosheets as efficient photosensitizers and pH-responsive drug nanocarriers for cancer imaging and therapy. *J. Mater. Chem. B* **2**, 1031 (2014).
94. Tiwari, J. N. *et al.* Accelerated Bone Regeneration by Two-Photon Photoactivated Carbon Nitride Nanosheets. *ACS Nano* **11**, 742–751 (2017).
95. Liao, G. *et al.* Emerging graphitic carbon nitride-based materials for biomedical applications. *Progress in Materials Science* **112**, 100666 (2020).
96. Thomas, A. *et al.* Graphitic carbon nitride materials: variation of structure and morphology and their use as metal-free catalysts. *J. Mater. Chem.* **18**, 4893 (2008).
97. Barrio, J., Volokh, M. & Shalom, M. Polymeric carbon nitrides and related metal-free materials for energy and environmental applications. *J. Mater. Chem. A* **8**, 11075–11116 (2020).
98. Hao, Q. *et al.* Graphitic carbon nitride with different dimensionalities for energy and environmental applications. *Nano Res.* **13**, 18–37 (2020).
99. Fan, X., Feng, Y., Su, Y., Zhang, L. & Lv, Y. A green solid-phase method for preparation of carbon nitride quantum dots and their applications in chemiluminescent dopamine sensing. *RSC Adv.* **5**, 55158–55164 (2015).
100. Patir, K. & Gogoi, S. K. Facile Synthesis of Photoluminescent Graphitic Carbon Nitride Quantum Dots for Hg2+ Detection and Room Temperature Phosphorescence.
101. Zhou, J., Yang, Y. & Zhang, C. A low-temperature solid-phase method to synthesize highly fluorescent carbon nitride dots with tunable emission. *Chem. Commun.* **49**, 8605 (2013).
102. Zhang, X. *et al.* Enhanced Photoresponsive Ultrathin Graphitic-Phase C_3N_4 Nanosheets for Bioimaging. *J. Am. Chem. Soc.* **135**, 18–21 (2013).
103. Wang, A., Wang, C., Fu, L., Wong-Ng, W. & Lan, Y. Recent Advances of Graphitic Carbon Nitride-Based Structures and Applications in Catalyst, Sensing, Imaging, and LEDs. *Nano-Micro Lett.* **9**, 47 (2017).
104. Zhang, Y. *et al.* Synthesis and luminescence mechanism of multicolor-emitting g-C3N4 nanopowders by low temperature thermal condensation of melamine. *Sci Rep* **3**, 1943 (2013).

105. Liu, J. *et al.* Carbon nitride nanosheets as visible light photocatalytic initiators and crosslinkers for hydrogels with thermoresponsive turbidity. *J. Mater. Chem. A* **5**, 8933–8938 (2017).
106. Kumru, B., Molinari, V., Dünnebacke, R., Blank, K. G. & Schmidt, B. V. K. J. Extremely Compressible Hydrogel via Incorporation of Modified Graphitic Carbon Nitride. *Macromol. Rapid Commun.* 1800712 (2018) doi:10.1002/marc.201800712.
107. Kumru, B. *et al.* Robust Carbon Nitride-Based Thermoset Coatings for Surface Modification and Photochemistry. *ACS Appl. Mater. Interfaces* **11**, 9462–9469 (2019).
108. Giusto, P., Kumru, B., Zhang, J., Rothe, R. & Antonietti, M. Let a Hundred Polymers Bloom: Tunable Wetting of Photografted Polymer-Carbon Nitride Surfaces. *Chem. Mater.* **32**, 7284–7291 (2020).
109. Zhao, F. *et al.* Supramolecular quantum dots as biodegradable nano-probes for upconversion-enabled bioimaging. *Chem. Commun.* **51**, 13201–13204 (2015).
110. Zheng, D.-W. *et al.* Carbon-Dot-Decorated Carbon Nitride Nanoparticles for Enhanced Photodynamic Therapy against Hypoxic Tumor *via* Water Splitting. *ACS Nano* **10**, 8715–8722 (2016).
111. Yan, S. C., Li, Z. S. & Zou, Z. G. Photodegradation Performance of g-C_3N_4 Fabricated by Directly Heating Melamine. *Langmuir* **25**, 10397–10401 (2009).
112. Glass, P., Chung, H., Washburn, N. R. & Sitti, M. Enhanced Reversible Adhesion of Dopamine Methacrylamide-Coated Elastomer Microfibrillar Structures under Wet Conditions. *Langmuir* **25**, 6607–6612 (2009).
113. Kang, S. *et al.* An instant, biocompatible and biodegradable high-performance graphitic carbon nitride. *Journal of Colloid and Interface Science* **563**, 336–346 (2020).
114. Papailias, I. *et al.* Chemical vs thermal exfoliation of g-C3N4 for NOx removal under visible light irradiation. *Applied Catalysis B: Environmental* **239**, 16–26 (2018).
115. Yang, H.-C., Chao, M.-W., Chou, C.-J., Wang, K.-H. & Hu, C. Mushroom waste-derived g-C3N4 for methyl blue adsorption and cytotoxic test for Chinese hamster ovary cells. *Materials Chemistry and Physics* **244**, 122715 (2020).
116. Aleksandrzak, M., Jedrzejczak-Silicka, M., Sielicki, K., Piotrowska, K. & Mijowska, E. Size-Dependent in Vitro Biocompatibility and Uptake Process of Polymeric Carbon Nitride. *ACS Appl. Mater. Interfaces* **11**, 47739–47749 (2019).
117. Vasilaki, E., Kaliva, M., Katsarakis, N. & Vamvakaki, M. Well-defined copolymers synthesized by RAFT polymerization as effective modifiers to enhance the photocatalytic performance of TiO 2. *Applied Surface Science* **399**, 106–113 (2017).
118. Parkatzidis, K. *et al.* Initiator-Free, Multiphoton Polymerization of Gelatin Methacrylamide. *Macromol. Mater. Eng.* **303**, 1800458 (2018).
119. Caliari, S. R. & Burdick, J. A. A practical guide to hydrogels for cell culture. *Nat Methods* **13**, 405–414 (2016).
120. Fan, C. & Wang, D.-A. Effects of permeability and living space on cell fate and neo-tissue development in hydrogel-based scaffolds: a study with cartilaginous model. *Macromol Biosci* **15**, 535–545 (2015).
121. Tsou, Y.-H., Khoneisser, J., Huang, P.-C. & Xu, X. Hydrogel as a bioactive material to regulate stem cell fate. *Bioactive Materials* **1**, 39–55 (2016).
122. Annabi, N. *et al.* Controlling the Porosity and Microarchitecture of Hydrogels for Tissue Engineering. *Tissue Engineering Part B: Reviews* **16**, 371–383 (2010).
123. Thakur, T. *et al.* Photocrosslinkable and elastomeric hydrogels for bone regeneration: PHOTOCROSSLINKABLE AND ELASTOMERIC HYDROGELS. *J. Biomed. Mater. Res.* **104**, 879–888 (2016).
124. Sadat-Shojai, M., Khorasani, M.-T. & Jamshidi, A. 3-Dimensional cell-laden nano-hydroxyapatite/protein hydrogels for bone regeneration applications. *Materials Science and Engineering: C* **49**, 835–843 (2015).

125. Lazić, S., Zec, S., Miljević, N. & Milonjić, S. The effect of temperature on the properties of hydroxyapatite precipitated from calcium hydroxide and phosphoric acid. *Thermochimica Acta* **374**, 13–22 (2001).
126. Fernando, S., McEnery, M. & Guelcher, S. A. Polyurethanes for bone tissue engineering. in *Advances in Polyurethane Biomaterials* 481–501 (Elsevier, 2016). doi:10.1016/B978-0-08-100614-6.00016-0.
127. Su, W. *et al.* Research Progress Review of Preparation and Applications of Fluorescent Hydrogels. *Journal of Chemistry* **2020**, 1–17 (2020).
128. Zhang, L., Liu, M., Zhang, Y. & Pei, R. Recent Progress of Highly Adhesive Hydrogels as Wound Dressings. *Biomacromolecules* **21**, 3966–3983 (2020).
129. Lin, K. T., Wang, A., Nguyen, A. B., Iyer, J. & Tran, S. D. Recent Advances in Hydrogels: Ophthalmic Applications in Cell Delivery, Vitreous Substitutes, and Ocular Adhesives. *Biomedicines* **9**, 1203 (2021).
130. Zingale, E. *et al.* Fluorescent Nanosystems for Drug Tracking and Theranostics: Recent Applications in the Ocular Field. *Pharmaceutics* **14**, 955 (2022).
131. Dong, Y. C., Bouché, M., Uman, S., Burdick, J. A. & Cormode, D. P. Detecting and Monitoring Hydrogels with Medical Imaging. *ACS Biomater. Sci. Eng.* **7**, 4027–4047 (2021).
132. Lin, J.-T., Liu, H.-W., Chen, K.-T. & Cheng, D.-C. Modeling the Kinetics, Curing Depth, and Efficacy of Radical-Mediated Photopolymerization: The Role of Oxygen Inhibition, Viscosity, and Dynamic Light Intensity. *Front. Chem.* **7**, 760 (2019).
133. Fonseca Parra, E. P., Chouchene, B., Six, J.-L., Schneider, R. & Ferji, K. Mechanistic Insights into Oxygen Tolerance of Graphitic Carbon Nitride-Mediated Heterogeneous Photoinduced Electron Transfer-Reversible Addition Fragmentation Chain Transfer Polymerization. *ACS Appl. Polym. Mater.* **3**, 3649–3658 (2021).
134. Moussa, H. *et al.* Growth of ZnO Nanorods on Graphitic Carbon Nitride gCN Sheets for the Preparation of Photocatalysts with High Visible-Light Activity. *ChemCatChem* **10**, 4973–4983 (2018).
135. Yang, L. *et al.* Two-channel photocatalytic production of H2O2 over g-C3N4 nanosheets modified with perylene imides. *Journal of Catalysis* **352**, 274–281 (2017).
136. Zhang, T., Yeow, J. & Boyer, C. A cocktail of vitamins for aqueous RAFT polymerization in an open-to-air microtiter plate. *Polym. Chem.* **10**, 4643–4654 (2019).
137. Su, F. *et al.* Aerobic Oxidative Coupling of Amines by Carbon Nitride Photocatalysis with Visible Light. *Angewandte Chemie International Edition* **50**, 657–660 (2011).
138. Sampaio, R. N., Grills, D. C., Polyansky, D. E., Szalda, D. J. & Fujita, E. Unexpected Roles of Triethanolamine in the Photochemical Reduction of CO_2 to Formate by Ruthenium Complexes. *J. Am. Chem. Soc.* **142**, 2413–2428 (2020).
139. Pellegrin, Y. & Odobel, F. Sacrificial electron donor reagents for solar fuel production. *Comptes Rendus Chimie* **20**, 283–295 (2017).
140. García-Peñas, A. *et al.* Effect of Hydrophobic Interactions on Lower Critical Solution Temperature for Poly(N-isopropylacrylamide-co-dopamine Methacrylamide) Copolymers. *Polymers* **11**, 991 (2019).
141. Vatankhah-Varnoosfaderani, M., Hashmi, S., GhavamiNejad, A. & Stadler, F. J. Rapid self-healing and triple stimuli responsiveness of a supramolecular polymer gel based on boron–catechol interactions in a novel water-soluble mussel-inspired copolymer. *Polym. Chem.* **5**, 512–523 (2014).
142. Andrzejewska, E. Chapter 2 - Free Radical Photopolymerization of Multifunctional Monomers.
143. Lee, T. Y., Guymon, C. A., Jönsson, E. S. & Hoyle, C. E. The effect of monomer structure on oxygen inhibition of (meth)acrylates photopolymerization. *Polymer* **45**, 6155–6162 (2004).

144. Patocka, J. & Hon, Z. Ethylene glycol, hazardous substance in the household. *Acta Medica (Hradec Kralove)* **53**, 19–23 (2010).
145. Winek, C. L., Shingleton, D. P. & Shanor, S. P. Ethylene and Diethylene Glycol Toxicity. *Clinical Toxicology* **13**, 297–324 (1978).
146. Mochida, K. & Gomyoda, M. Toxicity of ethylene glycol, diethylene glycol, and propylene glycol to human cells in culture. *Bull. Environ. Contam. Toxicol.* **38**, 151–153 (1987).
147. Niu, J., Lunn, D., Pusuluri, A. *et al.* Engineering live cell surfaces with functional polymers via cytocompatible controlled radical polymerization. *Nature Chem* **9**, 537–545 (2017). https://doi.org/10.1038/nchem.2713
148. Implantation of encapsulated biological materials for treating diseases. D Scharp, P Latta, C Yue, X Yu, JA Hubbell. ***US Patent 7,427,415, 2008***.